

Reaction Studies of Neutral Atomic C with H_3^+ using a Merged Fast-Beams Apparatus

A. P. O'Connor^{1,2}, X. Urbain³, J. Stützel^{1,4}, K. A. Miller¹, N. de Ruelle¹, M. Garrido¹,
and D. W. Savin¹

savin@astro.columbia.edu

ABSTRACT

We have investigated the chemistry of $\text{C} + \text{H}_3^+$ forming CH^+ , CH_2^+ , and CH_3^+ . These reactions are believed to be some of the key gas-phase astrochemical processes initiating the formation of organic molecules in molecular clouds. For this work we have constructed a novel merged fast-beams apparatus which overlaps a beam of molecular ions onto a beam of ground-term neutral atoms. Here we describe the apparatus in detail and present cross section data for forming CH^+ and CH_2^+ at relative energies from ≈ 9 meV to ≈ 20 and 3 eV, respectively. Measurements were performed for statistically populated $\text{C}(^3P_J)$ in the ground term reacting with hot H_3^+ (at an internal temperature of $\sim 2,550$ K). Using these data we have derived rate coefficients for translational temperatures from ≈ 72 K to $\approx 2.3 \times 10^5$ and 3.4×10^4 K, respectively. For the formation of CH_3^+ we are able only to put an upper limit on the rate coefficient. Our results for CH^+

¹Columbia Astrophysics Laboratory, Columbia University, New York, NY 10027, U. S. A.

²Present address: Max-Planck Institute for Nuclear Physics, Heidelberg 69117, Germany

³Institute of Condensed Matter and Nanosciences, Université Catholique de Louvain, Louvain-la-Neuve B-1348, Belgium

⁴Present address: Bosch Engineering GmbH, Robert-Bosch-Allee 1, 74232 Abstatt, Germany

and CH_2^+ are in good agreement with the mass-scaled results from a previous ion trap study of $\text{C} + \text{D}_3^+$, at a translational temperature of $\sim 1,000$ K. That work also used statistically populated $\text{C}(^3P_J)$ but internally cold D_3^+ (~ 77 K). The good agreement between the two experiments implies that the internal excitation of the H_3^+ is not significant so long as the reaction proceeds adiabatically. At 300 K, the C fine-structure levels are predicted to be essentially statistically populated, enabling us to compare our translational temperature results to thermal equilibrium calculations. At this temperature our rate coefficient for forming CH^+ lies a factor of ~ 2.9 below the Langevin rate coefficient currently given in astrochemical databases and a factor of $\sim 1.8 - 3.3$ below the published classical trajectory studies using quantum mechanical potential energy surfaces. Our results for CH_2^+ formation at 300 K are a factor of ≈ 26.7 , above these semi-classical results. Astrochemical databases do not currently include this channel. We also present a method for converting our translational temperature results to thermal rate coefficients for temperatures below ≈ 300 K. The results indicated that CH_2^+ formation dominates over that of CH^+ at temperatures $\lesssim 50$ K.

Subject headings: Astrobiology – Astrochemistry – ISM: molecules – Methods: laboratory – Molecular data – Molecular processes

1. Introduction

The first organic molecules are thought to have formed through interstellar gas-phase chemistry when atomic carbon was “fixed” into hydrocarbons. Typical molecular cloud densities are so low that one needs only consider binary collisions. As a result, the initial chemical network involved is rather simple, primarily consisting of C^+ or C reacting with either H, H_2 , or H_3^+ (van Dishoeck 1998; Herbst & Millar 2008). The cosmic pathway from

there to more complex hydrocarbons and other organic molecules passes through the molecular cations CH_n^+ ($n = 1 - 3$). Understanding how C^+ and C react to form these ions is therefore critical for modeling the origins of organic chemistry.

The available pathways for the C^+ network have been well laid out (van Dishoeck 1998; Herbst & Millar 2008), even if significant uncertainties remain in the actual rate coefficients (Vasyunin et al. 2008; Wakelam et al. 2009, 2010). Naively one would expect the hydrogen abstraction reaction



to be important. However, this process is endothermic by 0.4 eV and does not go forward at the low temperatures typical of molecular clouds. Instead, C^+ is thought primarily to undergo radiative association via



A discussion of theoretical and experimental work on this system can be found in Gerlich & Horning (1992) and Gerlich (2008) and references therein. Hydrogen abstraction reactions of the product CH_2^+ with H_2 can then form CH_3^+ . Recent experimental studies of hydrogen abstraction involving CH^+ and CH_2^+ have been published by Gerlich et al. (2011).

The corresponding C chemistry is expected to be dominated by reactions with H_3^+ , but the network is much more uncertain. Astrochemical databases currently include the proton transfer process (Wakelam et al. 2012; McElroy et al. 2013)



Classical trajectory studies using quantum mechanical potential energy surfaces (PESs) have been used to calculate the thermal rate coefficient for this reaction in the range of 10 – 300 K (Talbi et al. 1991; Bettens & Collins 1998, 2001). That semi-classical work takes into account

the temperature dependence of both the translational motion and the internal energy of the C atom but assumes the H_3^+ ion is in the ground state.

Ion trap measurements for



have been performed by Savić et al. (2005) at an estimated translational temperature of $\sim 1,000$ K (see Section 9.2 for a discussion of both the translational and internal temperatures in their work). Throughout this paper, we use the term “translational temperature” to refer to the reaction center-of-mass velocity distribution when it is described by a Maxwell-Boltzmann distribution. The internal energies of the reactants, however, are not necessarily in thermal equilibrium. When both the translational temperature and internal energies are in thermal equilibrium, we use the term “thermal”.

Comparing theory and experiment for these analogous reactions touches on a major issue in astrochemistry, namely how to convert data between isotopologues of a collision system. Two approaches are commonly used. Some researchers assume the rate coefficients are the same, independent of the isotopologues involved (e.g., Rodgers & Millar 1996; Albertsson et al. 2013). Others use the Langevin theory (Gioumousis & Stevenson 1958) and scale by the square root of the ratio of the reduced masses (e.g., Stancil et al. 1998; Gay et al. 2011). These two approaches result in a multiplicative scaling factor of 1 and 1.29, respectively, for the Savić et al. (2005) data. However, even taking this into account, theory and experiment have still not converged in either magnitude or temperature dependence. The theoretical calculations differ from one another by a factor of about 1.7. Including the error bars on the laboratory work, the published rate coefficients for this reaction span nearly an order of magnitude; though it is unclear if this represents a temperature dependence in the reaction or is a true discrepancy. But even assuming only a factor of 2 uncertainty, astrochemical sensitivity studies still find that improving the accuracy of this rate coefficient is of

critical importance for reliably matching model predictions to observations (Vasyunin et al. 2008; Wakelam et al. 2009, 2010).

Current astrochemical databases, however, do not consider the possibility of the additional $\text{C} + \text{H}_3^+$ reaction channels



and



If these reactions are fast enough, then they could result in an increased efficiency for the gas-phase formation of complex hydrocarbons. However, the theoretical predictions and experimental findings for these two reactions are not in agreement.

For reaction (5), Talbi et al. (1991) calculate that it possesses a significant activation energy and will not proceed at typical molecular cloud temperatures. Bettens & Collins (1998, 2001), though, find that the reaction proceeds with no barrier at a rate a factor of $\sim 60 - 110$ smaller than that for reaction (3). That this channel is open is supported by the experimental work of Savić et al. (2005) on the analogous system



However, they measure a rate coefficient that is only a factor of ~ 2 smaller than that for reaction (4).

As for reaction (6), it was not considered by either Talbi et al. (1991) or Bettens & Collins (1998, 2001). Quite likely that is because in binary collisions the process can only proceed via radiative association. Such reactions typically have rate coefficients many orders of magnitude smaller than processes such as reactions (3) and (4), which are expected to proceed with near Langevin rate coefficients (e.g., Herbst & Millar 2008). Surprisingly though, Savić et al.

(2005) measured a rate coefficient for the analogous process



and found that it is a factor of only ~ 12 smaller than that for reaction (4).

It is clear that additional research is needed to improve our understanding of the $\text{C} + \text{H}_3^+$ reaction complex. However, to accomplish this goal, there are formidable challenges both theoretically and experimentally.

Astrochemical databases use the Langevin value for the $\text{C} + \text{H}_3^+$ reaction system. The only detailed calculations of which we are aware for this system are the semi-classical results of Talbi et al. (1991) and Bettens & Collins (1998, 2001). Fully quantum mechanical scattering calculations for ion-neutral collision systems with 4 or more atoms appear to be just beyond current theoretical capabilities. The deep potential wells require large reactant and product basis sets. Accurate long-range potentials are needed as they are predicted to drive the reaction process. Additionally, multiple electronic surfaces may be involved along with non-adiabatic coupling between the surfaces. Brief reviews of the field can be found in Althorpe & Clary (2003) and Bowman et al. (2011). In the meanwhile, the state-of-the-art seems to be represented by the work of Klippenstein et al. (2010), which is a combination of transition state theory, classical trajectory simulations, and master equation analysis. They calculated the $\text{O}(^3P) + \text{H}_3^+$ and $\text{CO} + \text{H}_3^+$ systems; but we are unaware of any similar work on $\text{C}(^3P) + \text{H}_3^+$.

Experimentally, studies of cross sections and rate coefficients for reactions of C with molecular ions are extremely difficult. Part of the difficulty has to do with the challenge of generating beams of neutral atomic C. Standard experimental techniques for measuring ion-neutral reactions, such as flowing afterglows and related approaches, cannot generate sufficient amounts of neutral atomic C due to its high reactivity (A. Viaggiano, private communication). Laser ablation can produce beams of atomic C (Kaiser & Suits 1995; Gu et al.

2006), but have yet to be used in an experimental configuration that can generate cross sections or rate coefficients (Wilson et al. 2012). In fact, we are aware of only two published laboratory measurements of cross sections or rate coefficients for reactions of C with molecular ions (Schuette & Gentry 1983; Savić et al. 2005).

The approach of Schuette & Gentry (1983) was to send a fast beam of C^+ through a gas cell, neutralizing a portion of the beam through electron capture. After the cell, any remaining C^+ was magnetically removed, leaving a beam of neutral C. Merging an internally hot D_2^+ beam with the neutral beam, they studied the reaction



Because both beams were fast, standard laboratory methods could be used to characterize the parent beam profiles and particle currents and also to detect the product ions. Hence it was possible to perform absolute cross section measurements. However, the neutral C beam contained an unknown mixture of ground state and metastable levels of C with internal energies of up to ~ 4.2 eV. This limits the ability to make an unambiguous comparison of the results with theoretical calculations. Moreover, it also prevents the use of the results for astrochemistry where any neutral C atoms are expected to be in the ground term.

Another experimental approach taken is that of Savić et al. (2005). They used heated graphite rods to create an effusive beam consisting of a mixture of C, C_2 , and C_3 , which flowed into an ion trap containing internally cold D_3^+ . With their apparatus they investigated reactions (4), (7), and (8). Rate coefficients were determined by measuring the trapped parent and daughter ion populations versus time. However, there are a number of drawbacks to this method: (a) the beam is not pure and the C_n impurities ($n \geq 2$) can react with the trapped ions, potentially affecting the results; (b) the carbon source emits vacuum ultraviolet radiation which can cause ionization in the trap and alter the chemistry occurring; (c) the carbon beam is emitted in bursts and has an unknown density which varies spatially and

temporally, complicating the determination of the neutral-ion overlap and the extracted rate coefficient; (d) the energy of the carbon atoms and the energy spread of the effusive beam are both highly uncertain; and (e) the $\sim 1,000$ K translational temperature of the experiment is a factor of $\gtrsim 100$ higher than typical molecular cloud temperatures. However, perhaps the biggest issue is that (f) trapped ionic end products can undergo subsequent parasitic reactions with either parent-beam or background-gas neutrals, complicating the interpretation and analysis of the data. This last point is the reason that only lower limits were given for the error bars on their measurements of reactions (7) and (8).

It is clear that there is a need for an improved ability to study reactions of neutral atomic C with molecular ions. Here we describe a novel, merged fast-beams apparatus that we have developed to study such reactions. For our proof-of-principle studies we have investigated reactions (3), (5), and (6). As we describe below, our approach overcomes many of the limitations of Schuette & Gentry (1983) and Savić et al. (2005).

The rest of this paper is organized as follows. In Section 2 we review our experimental approach. A detailed description of the apparatus is provided in Section 3. Section 4 discusses the beam profile measurements and simulations used to determine the relative energies. Section 5 outlines how the signal was determined while Section 6 reviews the data acquisition method. Uncertainties and data averaging are briefly discussed in Section 7. Results are presented in Section 8 and discussed in Section 9. Some astrochemical implications are explored in Section 10. In Section 11 we summarize our findings.

2. Experimental Approach

We have developed a versatile merged fast-beams apparatus capable of studying a range of chemical processes involving neutral atoms or molecules reacting with atomic or molec-

ular ions (see Figure 1). As currently configured, the system is designed to detect charged daughter products which are heavier than either of the parent beams, such as reactions (3), (5), and (6).

The neutral beam portion of the apparatus begins with a Cs-ion sputter source to generate singly charged anions. By floating the source cathode to a negative potential of U_s , we non-selectively extract anions and generate a fast beam with a laboratory kinetic energy of $-eU_s$, where e is the unit charge. A Wien filter is used to purify the beam by selecting for the charge-to-mass ratio of the desired ion, which is then directed into an electrically isolated cell, floated to a potential of U_f . Inside this floating cell the anions, now with an energy of $-e(U_s - U_f)$, are crossed by a laser beam which photodetaches a fraction of the beam. After exiting the photodetachment chamber, the anions are electrostatically deflected into a Faraday cup, resulting in a neutral beam with a kinetic energy of $E_n = -e(U_s - U_f)$. For the second beam in the experiment, we use a duoplasmatron ion source floated to a positive potential of U_d . We select the desired cations with a Wien filter. The resulting ion beam kinetic energy is $E_i = eU_d$. An electrostatic deflector is used to merge the ions with the neutral beam.

For mono-energetic beams, the relative energy in the center-of-mass is given by (Brouillard & Claeys 1983)

$$E_r = \mu \left(\frac{E_n}{m_n} + \frac{E_i}{m_i} - 2\sqrt{\frac{E_n E_i}{m_n m_i}} \cos \theta \right). \quad (10)$$

where m_n and m_i are the neutral and ion masses, respectively; $\mu = m_n m_i / (m_n + m_i)$ is the reduced mass of the collision system; and θ is the intersection angle. This relative energy between the two beams can be controlled by varying either the source potentials or the floating cell potential or some combination thereof.

The beginning of the interaction region is determined by the point inside the electrostatic deflector where the ions merge with the neutral beam. A beam profile monitor (BPM) is

mounted near the beginning of the interaction region and another near the end. These are used to measure the horizontal and vertical profile of each beam and determine their overlap. During data acquisition, both beams are chopped on and off, out of phase. This enables us to extract the desired signal from various backgrounds. Parent beam densities of $\sim 10^4 - 10^5 \text{ cm}^{-3}$ help reduce to insignificant any possible effects of three-body and parasitic reactions.

The end of the interaction region is determined by an electrostatic chicane (Figure 2) which sends the parent ions into a Faraday cup, while the parent neutral beam continues ballistically and any heavier, charged daughter products are directed into an electrostatic energy analyzer. A hole in this analyzer allows the neutral beam to pass through into a detector which measures the neutral beam particle current. The desired product ion is selected based on its final kinetic energy and directed into a channel electron multiplier (CEM) operated in pulse counting mode. We note that, as a result of the high beam velocities in the laboratory frame, the angular spread of the reaction products is strongly compressed in the forward direction onto a small surface area. This enables us to use standard detection techniques to collect the signal ions emitted over the entire 4π steradians in the center-of-mass frame.

Experimentally we measure the reaction cross section σ times the relative velocity v_r convolved with the relative velocity spread of the experiment. This merged-beams rate coefficient can be written as (e.g., Bruhns et al. 2010b)

$$\langle \sigma v_r \rangle = \frac{S}{T_a T_g \eta} \frac{e^2 v_n v_i}{I_n I_i} \frac{1}{L \langle \Omega(z) \rangle}. \quad (11)$$

Here S is the count rate measured at the CEM, T_a is the transmittance of the analyzer for the selected daughter product, T_g is the geometric transmittance of the grid in front of the CEM, η is the CEM efficiency, v_n is the neutral beam velocity, v_i is that of the ion beam, I_n is the neutral particle current measured in amperes, I_i is the ion current, and L is the length

of the interaction region. The term $\langle\Omega(z)\rangle$ is the average overlap integral in the interaction region and is discussed further in Section 4.1.

Because we measure all of the quantities on the right hand side of Equation (11), we are able to report absolute measurements. From a combination of beam profile measurements and trajectory models, we are able to determine the interaction relative energy spread. This enables us to deconvolve our results to generate cross sections which can then be reconvolved with a Maxwell-Boltzmann distribution to generate a translational temperature rate coefficient.

3. Apparatus Description

The apparatus design is based, in part, on that of our self-merged fast-beams apparatus which has already been described in a series of papers (Kreckel et al. 2010; Bruhns et al. 2010a,b). For example, many of the ion optics for steering and focusing are similar to those used previously. Here we describe only those additional details specific to this new apparatus.

3.1. Carbon Beam Line

We generate a beam of C^- using a Cs-ion sputter source in combination with a Wien filter to remove all other unwanted negative particles. The Wien filter can readily resolve $^{12}C^-$ from both $^{13}C^-$ and $^{12}C^1H^-$, thereby enabling us to generate an isotopically pure $^{12}C^-$ beam. Generally we operate the beam at a relative energy of $E_{C^-} \approx 28$ keV. The full width half maximum (FWHM) energy spread for a C^- beam from a sputter source is typically ~ 15 eV (Doucas 1977a,b). Operating pressures in the region of the ion source are $\sim 10^{-6}$ Torr.

C^- is one of the rare atomic anions which possess more than one stable bound level lying below the first detachment threshold: a ground $2s^22p^3\ ^4S_{3/2}$ level and two excited $2s^22p^3\ ^2D_J$ levels ($J = 5/2$ and $3/2$). However, sputter sources have been shown to produce insignificant populations of the 2D_J excited levels (Scheer et al. 1998; Takao et al. 2007). Thus we produce an essentially pure beam of ground level C^- .

After exiting the Wien filter, the beam is directed into a 90° electrostatic cylindrical deflector. This deflection prevents any neutral particles or ultraviolet photons emitted by the source from having a direct path into the interaction region. Typical pressures in the deflector are $\sim 10^{-8}$ Torr. Nominal C^- currents after this deflector are $\sim 1.8\ \mu A$.

The anion beam is then directed through a 5 mm diameter circular aperture and continues essentially ballistically. Along this second leg of the carbon beamline, we have installed horizontal and vertical solenoid coils with rectangular cross sections. These enable us to largely cancel out the effects of the Earth’s magnetic field, which would generate an unwanted deflection of the anion beam.

After the 5 mm aperture, the anions enter into the floating cell, housed in what we call the photodetachment chamber. Outside of this chamber we use a diode laser to generate an 808-nm (1.53-eV) laser beam with ≈ 1.8 kW of power. Using lenses and mirrors external to the vacuum chamber, the beam is directed into the floating cell. Near the center of the overlap region with the anion beam, the laser light is brought to an oval-shaped focus where 90% of the power lies in an area of 9.4 mm in the horizontal direction and 11.6 mm in the vertical direction. The laser crosses the anions at an angle of $\phi \approx 2.74^\circ$. The laser beam exits the chamber a distance of 2008 mm from the entrance and is directed into a water-cooled power meter, which we monitor during data acquisition.

Based on the known photodetachment cross section (Seman & Branscomb 1962; Zhou et al. 2004), laser power, and anion velocity, and using the expected beam shapes and overlap ge-

ometry, we estimate that $\sim 4\%$ of the C^- beam is photodetached into ground term $C(^3P)$, though not all of the beam passes through subsequent apertures in the system. The photon energy and flux are insufficient to photodetach into higher lying levels of atomic C.

Based on previous photodetachment studies, we expect to statistically populate all three fine-structure J levels of the 3P ground term (Scheer et al. 1998). The $J = 1$ and 2 levels lie above the $J = 0$ ground level by energies of $E_J = 2.0$ and 5.4 meV, respectively. We have calculated the thermal population of the J levels using the partition functions

$$u_J = \frac{g_J e^{(-E_J/k_B T)}}{\sum_J g_J e^{(-E_J/k_B T)}}, \quad (12)$$

where $g_J = 2J + 1$ is the statistical weight of level J . The results are shown in Figure 3, which indicates that the fine-structure population reaches a statistical distribution for temperatures $\gtrsim 300$ K. We will return to this issue in Section 9.

The neutral beam exits the floating cell with a relative energy of $E_C = E_{C^-} + eU_f$. Both the anion and neutral beams then enter a 90° cylindrical deflector. The remaining C^- ions are electrostatically deflected into a Faraday cup which collects the anion beam. Typical C^- currents measured at this point are on the order of $1 \mu\text{A}$.

The neutral beam then passes through a 12 mm diameter aperture in the outer plate of this cylindrical deflector and after that through a second 5 mm aperture, a distance of 3168 mm downstream from the first. The separation of these two 5 mm apertures geometrically limits the divergence of the C beam to a maximum half angle of 1.57 mrad. The beam continues into yet another cylindrical electrostatic deflector and passes through a 12 mm diameter hole in the outer plate of that deflector. This deflector is used to merge the molecular ions with the neutral beam. For data acquisition, we chop the C beam on and off by chopping the laser beam. The switching time of the laser is on the order of a few hundred ns.

3.2. Molecular Beam Line

The molecular ions are formed using a duoplasmatron. We extract a beam of cations from the source and use a Wien filter to select the desired H_3^+ ions. The typical beam kinetic energy is $E_{\text{H}_3^+} \approx 7.05$ keV, chosen to match the laboratory velocity of the ≈ 28 keV C beam. The typical energy spread from a duoplasmatron has a FWHM of ~ 10 eV (Aberth & Peterson 1967). The pressure in the vicinity of the source is $\sim 10^{-6}$ Torr.

The vibrational and rotational temperatures of H_3^+ formed in a duoplasmatron may be quite substantial. This is due to the formation mechanism, namely, proton transfer between H_2^+ and H_2 , at least one of which is typically vibrationally excited in the discharge. Internal energies of $E \sim 1$ eV are inferred by Anicich & Futrell (1984). These are supported by experimental studies which found internal energies ranging between $\sim 0.5 - 1$ eV, with a generally decreasing internal energy as the source load pressure increases (X. Urbain, private communication). We convert this to an internal temperature using the theoretical partition function results of Kylänpää & Rantala (2011), specifically their Equation (8). Based on this, we estimate that our H_3^+ internal temperature lies between $\sim 2,200$ and $3,400$ K, which is below the $4,000$ K dissociation temperature of the system. The internal temperature is higher than that expected for many astrochemical environments. However, as we show later, this internal excitation appears not to have a significant effect on our measurements down to temperatures of at least ≈ 300 K. Still, in future work we hope to explore the possibility of installing a cold molecular ion source on our system.

As in the C beamline, the H_3^+ beam is deflected 90° into a second leg which is surrounded by rectangular shaped solenoid coils to cancel the magnetic field of the Earth in the horizontal and vertical directions. The beam is then directed into a drift region defined by two 5 mm apertures separated by a distance of 3069 mm. The drift region contains only two electrostatic ion optics, both just prior to the second aperture. The first is a horizontal

electrode, dubbed the “kicker”. This is used to adjust the vertical angle of the beam entering the 90° deflector which merges them onto the neutrals. With this we are able to reduce the vertical angle between the ion beam and the neutral beam in the interaction region. The second electrode is a horizontal plate opposite the kicker which we use to chop the beam, allowing or preventing the beam from being sent into the merger. The potential on this electrode is controlled using a fast high voltage switch with a switching time of better than 100 ns. This enables us to chop the H_3^+ beam on and off during data acquisition.

Typical H_3^+ currents exiting the drift region are ~ 250 nA. The divergence of the H_3^+ beam at this point is geometrically constrained by the collimating apertures, which limit the maximum half angle to 1.62 mrad. The beam then passes through a one-dimensional (1D) electrostatic lens and into a 90° electrostatic cylindrical deflector which merges the cations with the neutrals. The 1D lens is used to compensate for the focusing effects of the cylindrical deflector in the horizontal or merging plane. The divergence of the beam grows somewhat due to self-repulsion from space charge effects within the beam and due to focusing effects from the merging cylindrical deflector. Typical pressures in the beam merger are $\sim 10^{-8}$ Torr.

3.3. Interaction Region

The H_3^+ beam is brought horizontally onto the neutral C beam, near the exit of the beam merger. The two beams then co-propagate for some distance with a low relative velocity. Within this interaction region, some of the parent cations and neutrals undergo chemical reactions, generating daughter molecular ions.

The kinetic energy of the daughter ions is essentially the sum of E_C plus the product of the H_3^+ kinetic energy per amu (~ 2.35 keV amu $^{-1}$) times the mass in amu, transferred

from the H_3^+ . For matched parent-beam laboratory velocities, this typically corresponds to ≈ 30.35 keV for forming CH^+ , ≈ 32.70 keV for CH_2^+ , and ≈ 35.05 keV for CH_3^+ . These are the end products for reactions (3), (5), and (6), respectively. The dominant background ion is the ~ 28 keV C^+ formed when the parent C beam is ionized by collisions with residual gas in the vacuum system.

The parent beams are demerged using an electrostatic chicane. Trajectory studies using the ion optics package SIMION¹ indicate that the overlap length of the two beams is 1215 ± 25 mm. This distance includes both the merging and demerging regions, which make up less than 6% of the interaction length. The beams merge with an initial angle in the horizontal plane of 0.21 ± 0.01 rad and are brought parallel within a distance 30 mm. The demerging occurs in the vertical direction over a distance of 38 mm with a final angle between the beams of 0.19 ± 0.01 rad. Here and throughout all uncertainties are quoted at an estimated 1σ statistical confidence level.

The profiles of the C and H_3^+ beams are measured at distances of 280 and 1090 mm from the beginning of the interaction region (Figure 4). A retractable Faraday cup near the middle of the interaction region can be used to measure ion beam currents. The operating pressure in the interaction region is generally $\sim 10^{-8}$ Torr. To minimize any deflection of the parent and daughter product beams due to external magnetic fields, the interaction region is shielded using a series of solenoid coils, similar to the configuration in both the C and H_3^+ legs.

¹www.simion.com

3.4. Signal Detection

One of the challenges of this research is separating the daughter ions from the parent beams as well as from any unwanted background. We accomplish the desired discrimination using electrostatic ion optics, which allows us to analyze the beams based on their kinetic energy.

The parent H_3^+ beam is demerged from the C beam by the first pair of deflector plates in the chicane and directed with essentially 100% efficiency into a Faraday cup where the current is measured during data acquisition. Typical currents are ~ 200 nA. This corresponds to H_3^+ beam densities of $\sim 10^5$ cm^{-3} . The subsequent three pairs of deflector plates in the chicane bring the product ions and background C^+ again onto the path of the neutral C beam.

The remaining neutrals and ions then continue into an electrostatic energy analyzer which consists of three 90° cylindrical deflectors in series. The neutral beam passes unaffected through a 12 mm diameter hole in the outer plate of the lower cylindrical deflector (LCD), and continues into a neutral detector which we monitor during data acquisition. The calibration of this detector is described in Section 3.5.

The cations are deflected vertically by the LCD, which directs the desired ions into the middle cylindrical deflector (MCD). The MCD deflects these ions perpendicular to their trajectories before and after the LCD. There is a hole in the outer plate of the MCD, behind which a Faraday cup is mounted. Thus, with no voltage on the MCD, we can measure the beam current at this point. Dubbed the upper cup, the transmittance from the interaction region to this Faraday cup is $T_u = 0.80 \pm 0.02$.

The upper cylindrical deflector (UCD) bends the selected ions another 90° in the same plane as that of the MCD, for a total of 180° in a single plane. We found that this 180° deflection was necessary in order to electrostatically separate C^+ , CH^+ , CH_2^+ , and CH_3^+

from each other. At the exit of the UCD, the selected ions are moving downwards in the laboratory.

Ions which are discriminated against will strike somewhere on the inside of the LCD, MCD, or UCD. The deflector plates of all three are coated with a fine layer of graphite to minimize both photon and secondary charged particle emission resulting from these undesired ions hitting the surfaces. Typical operating pressures, as measured near the MCD, are on the order of $\sim 10^{-9}$ Torr.

The transmittance through the Chicane, LCD, MCD, and UCD was optimized using a proxy C^- beam at kinetic energies similar to those predicted for the product CH_n^+ ions and with inverted plate voltage polarities. This was carried out prior to data acquisition by mounting a Faraday cup at the exit of the UCD. The transmittance was found to be $T_a = 0.73 \pm 0.02$.

For data collection we installed a CEM at the exit of the UCD. Ions were detected in single particle counting mode. In front of the CEM we have mounted a grid with a geometric transmittance of $T_g = 0.90 \pm 0.01$. A voltage of -200 V is applied to the grid to repel negative particles produced in any of the cylindrical deflectors. The CEM particle detection efficiency is discussed below in Section 3.6.

3.5. Neutral Current Measurement

Typical neutral particle currents, as measured in amperes, are ~ 30 nA. This corresponds to atomic C beam densities of $\sim 1.4 \times 10^4$ cm^{-3} . Beam fluctuations during data acquisition introduce an $\approx 5\%$ uncertainty in the measured I_C . These are treated as a statistical uncertainty.

Neutral currents are measured on a particle collecting cup which can be externally

configured either as a Faraday cup to measure ion currents directly or as a neutral detector to measure neutral particle currents via secondary negative particle emission. The transmission efficiency of a neutral beam from the interaction region to this cup was measured using a 28 keV C^- proxy beam and found to be $T_n = 0.94 \pm 0.02$.

The neutral C particle current, as measured in amperes, is given by

$$I_C = \frac{I_{ND}}{\gamma T_n}. \quad (13)$$

Here I_{ND} is the current measured on the neutral detector and γ is the secondary negative particle emission coefficient for ~ 28 keV C striking the detector.

We used collisional detachment of C^- to determine the γ of the neutral detector. Helium was leaked into the chicane. As C^- passed through the He, single and double electron detachment formed C and C^+ , respectively. Triple electron detachment was found to form insignificant currents of C^{++} for the He gas pressures used. The various anion and cation currents were measured in the MCD upper cup by selecting the appropriate polarities for the voltage on the LCD and setting the MCD voltages to zero.

From conservation of particle flux, we expect at a given He pressure p to have

$$I_{C^-}(p=0) = I_{C^-}(p) + I_C(p) + I_{C^+}(p), \quad (14)$$

where the subscripts label the beam currents, which are defined as positive quantities. This can be rewritten in terms of measured quantities as

$$\frac{I_{C^-}^u(p)}{T_u} = \frac{I_{C^-}^u(0)}{T_u} - \frac{I_{ND}(p)}{\gamma T_n} - \frac{I_{C^+}^u(p)}{T_u}, \quad (15)$$

where I^u are the currents measured in the upper cup and the other quantities have been defined previously. Due to the configuration of the LCD, either $I_{C^-}^u$ or $I_{C^+}^u$ can be measured simultaneously with I_{ND} , but not both. So it is useful to rearrange this equation as

$$I_{C^-}^u(p) = I_{C^-}^u(0) - I_{ND}(p) \left[\frac{T_u}{\gamma T_n} + \frac{I_{C^+}^u(p)}{I_{ND}(p)} \right]. \quad (16)$$

In order to determine γ , the currents $I_{C^-}^u$ and I_{ND} are measured simultaneously for a set of pressure values p_i . The same is done for the currents $I_{C^+}^u$ and I_{ND} but as a result of the coarse control of the leak valve into the chicane, these data are collected on a different grid of pressure values p_k . Each of these latter two currents are then fit to polynomials $P_{C^+}(p_k)$ and $P_{ND}(p_k)$, respectively, which allows us to interpolate the data onto the p_i pressure grid. Expressing the ratio $I_{C^+}^u(p)/I_{ND}(p)$ as the ratio of these polynomials then yields

$$I_{C^-}^u(p_i) = I_{C^-}^u(0) - I_{ND}(p_i) \left[\frac{T_u}{\gamma T_n} + \frac{P_{C^+}(p_i)}{P_{ND}(p_i)} \right]. \quad (17)$$

Using this equation, we perform a least squares fitting over the entire pressure range for the measured $I_{C^-}^u$ and I_{ND} data and treat the quantities $I_{C^-}^u(0)$ and γ as fitting parameters. Doing this we find $\gamma = 2.7 \pm 0.3$ where the $\approx 11\%$ uncertainty represents the run-to-run 1σ spread in the measured γ and is treated as a systematic uncertainty.

3.6. CEM Efficiency

We used a commercially available CEM to detect the ions resulting from the reactions studied. CEMs have been shown to have a detection efficiency of $\gtrsim 95\%$ for cations with incident kinetic energies above 2 keV amu⁻¹ (Crandall et al. 1975; Savin et al. 1995). To better quantify this, we have measured the detection efficiency of a CEM identical to that used for our chemical studies here. For this we used a beam of ~ 27 keV C⁺ (~ 2.25 keV amu⁻¹) as a proxy for the CH_n⁺ product ions (~ 2.33 keV amu⁻¹). These measurements were performed on a merged-beams apparatus at the Université catholique de Louvain. The apparatus and technique is described briefly below. A more technical description of the general apparatus used for calibration can be found in Staicu-Casagrande et al. (2004).

Starting with an electron cyclotron resonance (ECR) ion source, we extracted cations from the source and mass selected them to form a 25 keV beam of C⁺⁺. The beam was then

electrostatically deflected into a high vacuum region and into a floating cell. This deflection prevented any C^+ formed upstream from making it into the floating cell, as such ions had the wrong energy-to-charge ratio to be transmitted into the cell. The floating cell was held at potential of -2 kV, thus C^{++} ions entering the floating cell were accelerated to 29 keV. Inside the floating cell, a fraction of the C^{++} beam underwent electron capture to form 29 keV C^+ . C^{++} ions exiting the floating cell decelerated to 25 keV and the C^+ to 27 keV.

After the floating cell, both carbon charge states are then separated using an electro-magnet which directs the \sim nA 25 keV C^{++} current into a movable Faraday cup within the magnet and the \sim pA 27 keV C^+ current, generated in the floating cell, into a retractable Faraday cup at the exit of the magnet. The floating cell voltage shifts the energy-to-charge ratio, so that only those ions formed via electronic capture within the floating cell have the correct energy-to-charge ratio to reach the detector. Any C^+ current produced outside of the floating cell will have a kinetic energy of 25 keV and not be directed into the retractable Faraday cup. Comparing the two currents we found that $\approx 7.5 \times 10^{-4}$ of the C^{++} underwent electron capture to form C^+ . We then attenuated the C^{++} beam at the source to give an \sim pA C^{++} current as measured within the magnet. The changes in the source conditions had no measurable effect on the pressure in the floating cell or in the magnet. Hence, as we are in the single collision regime, it is safe to assume that the attenuated C^+ particle count rate should be given by $\approx (7.5 \times 10^{-4})I_{C^{++}}/e$. Comparing this predicted value to that measured on a CEM situated directly behind the retractable Faraday cup, we find the CEM efficiency to be $\eta = 0.99 \pm 0.03$.

4. Beam Overlap and Relative Energies

We have determined the overlap of the two beams through a combination of beam profile measurements and geometric modeling. The beam profiles are measured using the two BPMs

located in the interaction region. Typical profiles are shown in Figure 4. Simulations of the beam trajectories have been created based on the known experimental geometry and the measured beam profiles. These modeling studies are also used to determine the average relative energy $\langle E_r \rangle$ and the corresponding energy spread. The methodology employed is similar to that described by Bruhns et al. (2010a) and is only briefly reviewed here.

4.1. Beam overlap

The overlap between the two beams at an arbitrary position is given by

$$\Omega(z) = \frac{\iint J_n(x, y, z) J_i(x, y, z) dx dy}{\iint J_n(x, y, z) dx dy \iint J_i(x, y, z) dx dy}, \quad (18)$$

where J_n and J_i are the fluxes of the neutral and ion beams, respectively; z is chosen to lie along an axis defined by the propagating beams in the laboratory frame; and x and y are both perpendicular to the z axis and to one another. Bruhns et al. (2010a) explain how this is implemented experimentally using the BPM data to calculate $\Omega(z)$. These experimental values are used to constrain the geometric simulations described below. The geometric model enables us, in turn, to determine the average overlap factor in the interaction region

$$\langle \Omega(z) \rangle = \frac{1}{L} \int_0^L \Omega(z) dz, \quad (19)$$

which is needed for Equation (11).

4.2. Geometric Simulations

Particle ray tracing was computed starting from a pseudo-plane analogous to the end of the interaction region. In this Monte Carlo simulation, the particles were flown in reverse from this plane and through the limiting apertures of their respective beam lines. Each particle was given a random starting position and an initial trajectory in this pseudo-plane.

In addition, the kinetic energy for each particle was randomly assigned from a Gaussian probability distribution using the FWHM for the corresponding source.

4.2.1. *Beam Profiles*

Beam profiles were calculated from the simulated particle flux distribution at pseudo-plane analogs of the two BPM locations within the interaction region (see Figure 4). The profiles were derived along the lines of Equations (53) and (54) of Bruhns et al. (2010a). The simulated C beam profiles were found to be in good agreement with those measured. For the H_3^+ beam, it was necessary to adjust the shape and position of the limiting apertures used in the calculations in order for the simulated profiles to best match those measured. These adjustments were required to account for a vertical shift of the H_3^+ beam as it moved through the interaction region along with focusing effects induced by the beam merger, resulting in a typical average bulk misalignment of 0.81 mrad as determined from the beam profiles. SIMION studies indicate that these features are the result of a minor misalignment of the 1D lens prior to the 90° deflection which merges the H_3^+ onto the C beam.

From our Monte Carlo trajectory simulation, we can readily calculate $\Omega(z)$ using Equation (18). This is highly advantageous as it is not possible to measure the beam profiles along the entire interaction region. We use these simulations as a guide for interpolating $\Omega(z)$ between the BPMs and for extrapolating $\Omega(z)$ upstream and downstream of the BPMs.

4.2.2. *Relative Energies*

Calculating the particle relative energies from the Monte Carlo simulation required that the interaction region be discretized into pseudo-planes. In turn, each pseudo-plane was further divided into square cells. The size of the cells was selected so as to ensure

statistically significant particle densities. For every neutral-ion pair within each cell, we calculated the interaction angle and relative velocity. This process was repeated for every pseudo-plane. A typical simulation used 10,000 particles for each species with over 50 pseudo-planes, each divided into 900 cells. From these simulations, which take into account the bulk misalignment of the beam and their angular spreads, and binning the resulting interaction angles into a histogram, a Gaussian-like distribution emerged yielding a mean interaction angle of $\langle\theta\rangle = 1.16 \pm 0.46$ mrad.

A histogram for the calculated values of v_r throughout the interaction region is shown in Figure 5 for a small sample of floating cell voltages. For nearly velocity-matched beams $|U_f| \lesssim 50$ V, the relative velocity spread is dominated by the bulk interaction angle and the divergence of the two beams relative to one another. In this regime, the relative velocity spread is well described by a Maxwell-Boltzmann distribution². For floating cell values of $|U_f| \gtrsim 100$ V the relative velocity spread is determined largely by the energy spreads of the two ion sources. The resulting function tends towards a Gaussian distribution in velocity. The simulations also enable us to determine $\langle E_r \rangle$ versus U_f , along with the corresponding energy spread (see Figure 6). The simulations of the $C + H_3^+$ reaction complex studied here indicate that we achieved values of $\langle E_r \rangle$ as low as ≈ 9.3 meV, corresponding to an effective translational temperature of ≈ 72 K (as derived from a Maxwell-Boltzmann fit of the velocity distribution).

²More precisely we used the form for a three-dimensional Maxwell-Boltzmann velocity distribution as expressed in spherical coordinates and then integrated over θ and ϕ , leaving the relative velocity v_r as the sole remaining variable.

5. Signal Determination

The signal rate was extracted by accounting for the various backgrounds using a standard beam chopping technique (Brouillard & Claeys 1983). The neutral beam is chopped by turning the laser on and off. The timing of the laser is controlled using a programmable digital signal from the power supply unit (PSU). During typical operation the laser was gated on for 5 ms and off for 5 ms. The PSU also provides an external trigger. We sent this through a gate-and-delay generator and fed it into the fast high voltage switch that we use to chop the H_3^+ beam. The delay time is set to 2.5 ms or a quarter of the period for the laser chopping pattern. The resulting square wave pattern used is shown in Figure 7.

The CEM counts for each quadrant of the chopping cycle are recorded in four individual counter channels as

$$N_1 = N_C + N_b, \quad (20)$$

$$N_2 = N_S + N_C + N_{\text{H}_3^+} + N_b, \quad (21)$$

$$N_3 = N_{\text{H}_3^+} + N_b, \quad (22)$$

$$N_4 = N_b. \quad (23)$$

Here N_S represents the signal counts with both beams on, N_C is the background counts due to the C beam, $N_{\text{H}_3^+}$ is the background counts due to the H_3^+ beam, and N_b is the background counts with both beams off. The corresponding uncertainty in N_S from counting statistics is given by

$$\delta N_S = (N_1 + N_2 + N_3 + N_4)^{1/2}. \quad (24)$$

Data are collected at a given relative energy, for an integration time t . Taking the chopping pattern into account, the corresponding counter rates are readily calculated by dividing N_i by $t/4$, yielding R_i . The signal rate is then given by

$$S = R_2 - R_1 - R_3 + R_4 \quad (25)$$

where the fractional uncertainty in S is $\delta N_S/N_S$.

Figure 8 shows count rates R_1 through R_4 as a function of the UCD plate potential. For this the LCD and MCD voltages were already optimized for transmittance of the CH^+ signal. These rates have been normalized to the peak of the resulting signal rate scan, which is also shown in the figure. The largest of these beam-induced backgrounds occurs when the C beam is on. This background is due to C atoms stripping on residual gas and forming C^+ ions with a kinetic energy close to that of the CH^+ signal ions. A portion of the resulting C^+ ions are transmitted through the electrostatic energy analyzer system and into the CEM for UCD voltages just below those giving the optimal transmission of the CH^+ beam.

We confirmed the shape of the resulting signal scan using a proxy for the CH^+ signal. The proxy was generated by tuning the kinetic energy of the C^- beam to that expected for the CH^+ signal. Double electron detachment on residual gas in the apparatus generated a C^+ beam which we directed through the detector system and into a Faraday cup mounted at the CEM position. A comparison of the normalized proxy beam current is shown in Figure 9, along with the normalized signal counts. The transmitted profiles match closely, confirming that we have successfully removed the background from the signal. The proxy C^+ scan profile skews similar to the signal profile. We carried out experimental tests which confirmed that this is due to the beams entering the LCD from the chicane at a slight angle and a mismatch in applied plate voltages with respect to that required for ion transmission along the central trajectory of the cylindrical deflectors.

6. Data Acquisition Procedure

For a typical data acquisition cycle, the C^- and H_3^+ beams are first each tuned independently to optimize the transported current and beam profiles in the interaction region.

The beams are then tuned together to make them as parallel as possible. Once tuned, data acquisition begins. The data acquisition procedure is largely controlled via an automated LabVIEW program. For a typical data acquisition run, U_f is fixed and the signal counts N_S recorded until the statistical uncertainty $\delta N_S/N_S$ approaches $\sim 4\%$.

The floating cell voltage was scanned in steps of 50 V for $|U_f|$ between 0 and 500 V and from there in larger steps of 100 V up to 2.0 kV. In order to minimize focusing of the C^- beam by the floating cell, and hence of the C beam, we limited $|U_f|$ to voltages below 10% of the sputter source voltage, typically $|U_f| \leq 2$ keV. To achieve effective values of $|U_f|$ beyond 2.0 kV, the C^- ion source voltage was offset and U_f scanned in 200 V steps from 0 to 2.0 kV. Varying the voltage offset on the source enabled us to achieve effective values of U_f up to 4.0 kV. The upper limit was defined by the maximum stable source potential of ≈ 30 kV, combined with $U_f = 2$ kV. As a result, we were able to scan $\langle E_r \rangle$ between ≈ 9 meV and 20 eV.

Data acquisition for a typical data run begins with the control program measuring the C and H_3^+ beam profiles. While one beam is being profiled, the other is off. Beam chopping is then initiated and the beam currents measured. To within the stability of each beam, the chopped current measurement is half that of the unchopped beam. Next, all four counters are initialized and data are collected for an integration time of $t = 10$ s. The current measurements and 10-s integration are repeated typically 100 – 200 times. Afterwards, the chopping is turned off and the beam profiles are measured again. During the period between profile measurements, the beam currents are continually monitored and act as a proxy for the stability of the measurement and the alignment of the beams. The data acquisition cycle is repeated until either the statistical uncertainty approaches the desired level or the ion beams begin to de-tune.

7. Uncertainties and Averaging

Tables 1 and 2 list typical experimental operating values for the quantities going into Equation (11) and their associated uncertainties. The different terms are divided into those uncertainties which are statistical in nature (Table 1) and those which are systematic (Table 2). The signal data at a given relative energy were collected over a number of experimental runs until the counting-statistics uncertainty in S was typically less than 4%. More details about the various terms can be found in Sections 3-5.

For each data run i at a given $\langle E_r \rangle$, we calculated the measured merged-beams rate coefficient $\langle \sigma v_r \rangle_i$ and the associated statistical-like experimental uncertainty $\delta \langle \sigma v_r \rangle_i$. The various runs at that energy were averaged together using a weighting of

$$w_i = \frac{1}{(\delta \langle \sigma v_r \rangle_i)^2} \quad (26)$$

The resulting merged-beams rate coefficient and associated 1σ statistical-like uncertainty is then given by

$$\langle \sigma v_r \rangle = \frac{\sum_i \langle \sigma v_r \rangle_i w_i}{\sum_i w_i} \pm \left(\sum_i w_i \right)^{-1/2}. \quad (27)$$

There is an additional 12% systematic uncertainty on each resulting merged-beams rate coefficient.

8. Results

8.1. Experimental Merged-Beams Rate Coefficients

Figure 10 presents our experimental results for the merged-beams rate coefficient as a function of the average relative energy $\langle E_r \rangle$ for $\text{C} + \text{H}_3^+ \rightarrow \text{CH}^+ + \text{H}_2$, reaction (3), and for $\text{C} + \text{H}_3^+ \rightarrow \text{CH}_2^+ + \text{H}$, reaction (5). The error bars show the 1σ statistical-like uncertainty. We also searched for CH_3^+ signal from reaction (6): $\text{C} + \text{H}_3^+ \rightarrow \text{CH}_3^+ + \text{photon}$. However,

analyzer scans within the predicted kinetic energy range for the CH_3^+ signal yielded count rates indistinguishable from the background noise. At matched beam velocities, $\langle E_r \rangle = 9.3$ meV, the measured rate coefficient of $-0.657 \pm 6.42 \times 10^{-11} \text{ cm}^3 \text{ s}^{-1}$, enables us to put a 1σ upper limit of $5.76 \times 10^{-11} \text{ cm}^3 \text{ s}^{-1}$ on this channel.

8.2. Cross Sections

We have extracted the cross section from our data using the functional form

$$\sigma_x = \frac{a_0 + a_{1/2}E^{1/2}}{E^{2/3} + b_1E + b_2E^2 + b_4E^4}, \quad (28)$$

where x denotes either reaction (3) or (5). The resulting cross sections are in units of cm^2 for E in eV. Over the ranges for which data were measured, the fitting accuracy was between 2 – 6% for reaction (3) and 6 – 17% for reaction (5).

Concerning the first term of the denominator in Equation (28), leaving the power as a free fitting parameter yields an $E^{-0.7 \pm 0.1}$ behavior at low energies for CH^+ formation. For the case of CH_2^+ , we find an $E^{-0.3 \pm 0.3}$ behavior. We attribute the large uncertainty in this term to the rapid decrease of the CH_2^+ merged-beams rate coefficient with relative energy. As a result the fit is dominated by the higher order terms. Here, we have chosen to use $E^{-2/3}$ for both channels as it agrees to within the experimental uncertainties and for which there is some theoretical support. This term results in a thermal rate coefficient with a $T^{-1/6}$ behavior at low temperatures and matches the calculated behavior for the thermal rate coefficient of the electronically similar reaction complex $\text{O}(^3P) + \text{H}_3^+$, which is predicted to be dominated at low temperatures by the charge-quadrupole interaction (Klippenstein et al. 2010). The terms in the denominator with greater powers of E have been arbitrarily selected to match the higher energy dependence in each of the measured merged-beams rate coefficients.

The best fit parameters were derived using these functional forms for the cross sections,

multiplying them by v_r , convolving them with the experimental velocity distribution, and performing a χ^2 fit between the measured merged-beams rate coefficients and the model. The resulting best fits to the data are shown by the solid lines in Figure 10. For reaction (3) the fit is good over the measured relative energy range of ≈ 9 meV to 20 eV and for reaction (5) from ≈ 9 meV to 3 eV. The best fit parameters of the cross section for each reaction are given in Table 3. The experimentally derived cross sections for both reactions are plotted in Figure 11.

8.3. Translational Temperature Rate Coefficients

The translational temperature rate coefficient α_x , for reaction x , is derived by multiplying the extracted cross section σ_x by the relative velocity and convolving the product with a Maxwell-Boltzmann distribution. Using Equation (28) as a guide, we have fit our resulting rate coefficients with

$$\alpha_x = \frac{a_0 + a_{1/2}T^{1/2} + a_1T}{T^{1/6} + b_{1/2}T^{1/2} + b_1T + b_{3/2}T^{3/2}}, \quad (29)$$

where x denotes either reaction (3) or (5). The resulting rate coefficients are given in units of $\text{cm}^3 \text{ s}^{-1}$ for T in units of K. The best fit parameters for each reaction are given in Table 4.

The experimentally derived translational temperature rate coefficients are shown by the solid curves in Figure 12. The shaded regions show the quadrature sum of the systematic uncertainty and the fitting accuracy, yielding an uncertainty of between 12 – 13% for reaction (3) and between 14 – 18% for reaction (5). The low temperature limit for the validity of the derived translational temperature rate coefficients is ≈ 72 K, which is the effective translational temperature of our experimental energy spread for the minimum $\langle E_r \rangle$ achieved. The functional form of Equation (29) has been chosen so that the extrapolation below 72 K goes to a $T^{-1/6}$ behavior as predicted by Klippenstein et al. (2010) for the electronically similar reaction complex $\text{O}(^3P) + \text{H}_3^+$. The high temperature limits for the fits of $\approx 2.3 \times 10^5$

and 3.5×10^4 K correspond to the highest values of $\langle E_r \rangle$ measured for reactions (3) and (5) of ≈ 20 and 3 eV, where the cross sections are vanishingly small.

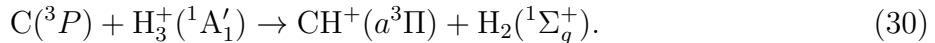
9. Discussion

An energy-level diagram for the various $\text{C} + \text{H}_3^+$ reaction pathways which we discuss in this section can be found in Figure 13. The sources for the derivation of this energy-level diagram are given in the figure caption.

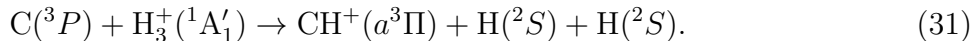
9.1. Merged-Beams Rate Coefficient

9.1.1. $\text{C} + \text{H}_3^+ \rightarrow \text{CH}^+ + \text{H}_2$

The neutral C is of 3P symmetry. H_3^+ is of $^1A'_1$ symmetry, as this is the only electronic state which lies below the dissociation limit of the molecule (McNab 1995). The final electronic state of H_2 is $^1\Sigma_g^+$. Hence, taking the spin multiplicities into account (i.e., ignoring possible intersystem transitions to the CH_3^+ singlet manifold), the lowest accessible symmetry of CH^+ is the $a^3\Pi$ electronic state (Talbi et al. 1991; Bettens & Collins 1998). Putting it all together we can re-write reaction (3) as



This reaction is exoergic by ≈ 0.92 eV (Delsaut & Liévin 2015). The only additional channel for CH^+ formation is the endoergic reaction:



The threshold for this reaction is ≈ 3.55 eV. Delsaut & Liévin (2015)

Our measured merged-beams rate coefficient for reaction (3) exhibits a relative energy

dependence that is similar to that measured by Schuette & Gentry (1983) for reaction (9): $C + D_2^+ \rightarrow CD^+ + D$. Figure 10 presents their cross section results multiplied by v_r . Both measurements show an initial increase in the merged-beams rate coefficient with increasing relative energy. Possible reasons for the similar behaviors seen with increasing energy could be due to the opening up of new electronic states in the intermediate reaction complex or to additional ro-vibrational channels becoming energetically accessible in the daughter products. Clearly, though, further theoretical and experimental work is needed to understand the observed behavior.

At some point, the magnitude of the rate coefficient dramatically decreases with increasing relative energy. We attribute this to the opening of additional reaction pathways that compete with the reaction we are measuring. The first four of these channels are:



with threshold energies of $\approx 1.98, 2.69, 4.32,$ and 6.16 eV, respectively (see Figure 13). In this relative energy range, we also see no obvious sign for the onset of CH^+ formation via reaction (31). We attribute this, in part, to the opening of the above competing channels.

A similar decrease was seen by Urbain et al. (1991) for the associative ionization (AI) reaction $H(1s) + H(2s) \rightarrow H_2^+ + e^-$. One difference, though, is that the cross section for the AI reaction shows a sharp and dramatic decrease at the opening of the competing $H(1s) + H(2s) \rightarrow H(1s) + H^+ + e^-$ channel. This is readily explained by the well-defined initial internal energies of the reactants and the absence of any internal degrees of freedom in their products.

In our results we cannot unambiguously identify the opening of any of the above channels competing with reaction (3). Moreover, the decrease seen in our data is not as sharp as that seen by Urbain et al. (1991). Both the shift and broadening of the observed threshold are most likely due to the H_3^+ internal excitation. The range of possible ro-vibrational levels that can contribute to the process effectively leads to a smearing out with relative energy, unlike what was seen by Urbain et al. (1991) for atomic collision partners. Additionally, the empirical fit to our data suggests that the merged-beams rate coefficient peaks at around 1.37 eV. This is about 0.61 eV below the opening of the first competing pathway at 1.98 eV, implying a level of internal excitation for the H_3^+ in our experiment that is in rough agreement with the predictions of Anicich & Futrell (1984) and the measurements of Urbain (private communication), which are discussed in Section 3.2. Using the partition function of Kylänpää & Rantala (2011), this 0.61 eV of excitation corresponds to an internal temperature of $\sim 2,500$ K.

9.1.2. $\text{C} + \text{H}_3^+ \rightarrow \text{CH}_2^+ + \text{H}$

Our results for reaction (5) show a decreasing merged-beams rate coefficient with increasing relative energy. Bettens & Collins (1998) describe the formation process of CH_2^+ as involving the rearrangement of the CH_3^+ complex followed by the ejection of one hydrogen atom. Using this as the basis of a hand-waving argument, we attribute the observed energy dependence to the decreasing time available for the rearrangement of the CH_3^+ complex as the collision energy increases. Clearly, though, further theoretical and experimental work will be needed to resolve this issue. Then at $\langle E_r \rangle \sim 1$ eV, similarly to that observed for reaction (3), the process rapidly decreases in strength. This suggests that we are seeing the onset of the competitive channels, reactions (32) to (35), but again shifted to a lower relative energy due to the internal excitation the H_3^+ in our measurement.

9.2. Translational Temperature Rate Coefficients

The reaction of ground-term C with cations is predicted by Gentry & Giese (1977) to be driven by the long-range shape of the PES. At these distances we do not expect the internal excitation of the H_3^+ to play any role. Based on these assumptions and the statistical population of the C fine-structure levels, we expect our translational temperature rate coefficient to be equivalent to a thermal equilibrium rate coefficient for $T \gtrsim 300$ K.

9.2.1. $\text{C} + \text{H}_3^+ \rightarrow \text{CH}^+ + \text{H}_2$

At 300 K, the Langevin rate coefficient adopted for this reaction by the astrochemical databases (Wakelam et al. 2012; McElroy et al. 2013) is a factor of ≈ 2.9 times larger than our results, while the semi-classical results of Talbi et al. (1991) and Bettens & Collins (1998, 2001) are larger by factors of ≈ 3.3 and ≈ 1.8 , respectively, as can be seen in Figure 12. The cause for the discrepancies is not immediately obvious. It is unlikely to be due to the differences in the population of the fine-structure levels in the atomic C, which are expected to be statistically populated in gas above 300 K as well as in our experiment. So it seems to us that a more likely explanation for the discrepancies is that the actual potential energy surfaces are less attractive than those used in the calculations, possibly due to an underestimate of the spin-orbit coupling strength (see Equations 6-10, Figure 4, and Appendix B of Klippenstein et al. 2010).

One might also be tempted to attribute these differences to the internal excitation of the H_3^+ ions used for the present results, as the calculations were performed for internally cold H_3^+ . However, a comparison to the work of Savić et al. (2005) strongly suggests that this is not the case. Our translational temperature rate coefficient is in very good agreement with the mass-scaled results of Savić et al. (2005). Their work used an effusive C beam, at

an estimated translational temperature of $T_C \sim 3,000$ K, colliding with D_3^+ stored in an ion trap, with wall temperatures of $T_{D_3^+} = 77$ K. Assuming that the D_3^+ cloud is approximately at rest with respect to the C beam, the translational temperature of the interaction T_t is given by

$$\frac{3k_B T_C}{2m_C} = \frac{3k_B T_t}{2\mu}, \quad (36)$$

yielding $T_t \sim 1,000$ K. The very good agreement between their work and ours suggests that at this translational temperature the internal excitation of the H_3^+ affects our results at a level constrained by the size of the mutual experimental uncertainties. We expect this to remain valid down to 300 K, as we can posit no reason for this situation to change so long as the fine-structure levels of the C remain statistically populated. Thus, at 300 K it seems unlikely that the differences between theory and our results can be attributed to internal excitation of the H_3^+ .

9.2.2. $C + H_3^+ \rightarrow CH_2^+ + H$

Our results indicate that there is no energy barrier for reaction (5) with internally excited H_3^+ . This is to be contrasted with the calculations of Talbi et al. (1991) who predict the existence of such a barrier. Later calculations by Bettens & Collins (1998, 2001) find no such barrier, but their predicted thermal rate coefficient lies a factor of ≈ 26.7 below our results at 300 K (see Figure 12). Results similar to ours were found by Savić et al. (2005) for internally cold D_3^+ . The very good agreement that we find between our work and their mass-scaled results suggests that indeed there is no barrier for this particular system.

Coming back to the work of Savić et al. (2005), they could not exclude the possibility of the deuterium-abstraction parasitic reaction



contributing to the formation of CD_2^+ . For that reason they gave only lower limits for their uncertainty on reaction (7). Such a parasitic reaction would effectively reduce their inferred CD^+ rate coefficient while boosting their CD_2^+ rate coefficient. In our experimental setup, the low density of the parent H_3^+ beam combined with the low CH^+ formation rate yields an insignificant rate for a parasitic reaction forming CH_2^+ . Hence, the good agreement between our results for reactions (3) and (5) and their mass-scaled results for reactions (4) and (7) suggest that, to within our mutual error bars, parasitic reactions were not an issue for their measurements of these two reactions.

9.2.3. $\text{C} + \text{H}_3^+ \rightarrow \text{CH}_3^+ + \text{photon}$

For radiative association to occur, the CH_3^+ collision complex must radiate away binding energy plus any internal energy of the parent H_3^+ ion. Based on our results for reaction (6), we can put a 1σ upper limit on the translational temperature rate coefficient at 72 K of $5.76 \times 10^{-11} \text{ cm}^3 \text{ s}^{-1}$, for an H_3^+ internal energy of $\sim 0.6 \text{ eV}$. The mass-scaled results of Savić et al. (2005) of $(5 \pm 3) \times 10^{-11} \text{ cm}^3 \text{ s}^{-1}$, lie within this limit, though their results are for the much higher translational temperature of $\sim 1,000 \text{ K}$ and with insignificant internal excitation of the H_3^+ . Still we find it unlikely that the rate coefficient for this reaction can be as high as their results suggest. Their data imply a surprisingly flat temperature dependence for this radiative association reaction. Moreover, previous experimental and theoretical studies for radiative association reactions have found rate coefficients many orders of magnitude smaller (Gerlich & Horning 1992). Savić et al. (2005) suggest that their results for this reaction may have been contaminated by parasitic reactions. For example, there is the two-step process of reaction (7) followed by the deuterium-abstraction reaction



or the three-step, and therefore less likely, process of reaction (4) followed by reaction (37) and then by reaction (38). The rate coefficient measured by Savić et al. (2005) can readily be explained if in their apparatus the effective rate coefficient for either of these two pathways was $\sim 10\%$ of the rate coefficient for the initial step. Unfortunately the uncertainty limits on their and our results do not enable us to tease out the explanation for their having measured such a high rate coefficient for this radiative association process.

9.3. Converting Translational Temperature to Thermal Rate Coefficients

Talbi et al. (1991) and Bettens & Collins (1998, 2001) carried out their calculations at 10 K. In their work, they treat the reaction adiabatically and ignore surface crossing and intersystem transitions. This approach is still standard for theoretical rate coefficients (Klippenstein et al. 2010; Li & Guo 2014). Additionally, Talbi et al. (1991) and Bettens & Collins (1998, 2001) extrapolated to temperatures up to 300 K by multiplicatively scaling their results to account for the temperature dependence of fractional populations of the attractive surfaces involved in the reaction. Here we take a similar approach. Using our translational temperature results on statistically populated ground-term C, we convert them to thermal rate coefficients using factors, derived below, which account for the temperature dependence of the fractional population of the attractive surfaces involved. In converting our translational temperature results to thermal data, we also ignore the internal excitation of the H_3^+ in our experiment. The role of internal excitation remains an open question for barrierless complex-forming reactions such as those studied here. Typically no enhancement in reactivity is expected (e.g., Guo 2012). However, experimental and theoretical work has shown that for some reactions internal excitation can significantly enhance reactivity (see Li & Guo 2014, and references therein). Our work cannot resolve this issue. But ignoring the H_3^+ internal excitation here seems a reasonable approximation based on the good agreement

between our results on hot H_3^+ and the mass-scaled results of Savić et al. (2005) on cold D_3^+ .

Gentry & Giese (1977) investigated reactions of ground-term atomic C with cations. That work used the adiabatic approximation in which the process is driven by the long-range shape of the PESs. The only aspect of the cation accounted for is the charge. They find that for ground-term C reacting with a cation, the nine states in the $\text{C}(^3P_J)$ manifold form six attractive surfaces and three repulsive. These can be characterized at long range by the J level and $|M_J|$ state of the carbon. The one state of the 3P_0 level and three states of the 3P_1 level correlate with attractive surfaces. For the 3P_2 level, two of the states correlate to attractive surfaces and three to repulsive.

Building on the work of Gentry & Giese (1977), Talbi et al. (1991) and Bettens & Collins (1998, 2001) have extended it to reactions with H_3^+ . They find that the reaction proceeds not through the singlet ground symmetry of CH_3^+ , but rather through excited triplet surfaces of the intermediate $\text{CH}^+ \cdot \text{H}_2$. In fact, in the reaction the C atom is predicted to be preferentially directed towards the apex of the H_3^+ triangle (cf., Figure 1 of Bettens & Collins 1998) The lowest energy triplet is the $^3A''$, which does not lie along the $\text{CH}^+ \cdot \text{H}_2$ reaction path. Complete rearrangement is needed to reach the $^3A''$ state, namely the insertion of the C atom between the three H nuclei.

Using the adiabatic approximation Talbi et al. (1991) and Bettens & Collins (1998, 2001) correlate the carbon fine-structure levels to the PESs of the $\text{CH}^+ \cdot \text{H}_2$ intermediate, namely the 3B_2 symmetry and the slightly higher 3B_1 symmetry, which are both attractive, while the next higher triplet symmetry, the 3A_2 is repulsive. The six attractive $\text{C} + \text{H}_3^+$ surfaces are assumed to correlate adiabatically with the six attractive surfaces formed by the 3B_2 and 3B_1 symmetries and the three repulsive $\text{C} + \text{H}_3^+$ surfaces to the three formed by the 3A_2 symmetry.

This leads to a one-to-one mapping of the long-range surfaces to those of the CH_3^+

intermediate. Using a $|J, |M_J|\rangle$ ket notation for the ground-term C, the $|0, 0\rangle$ state, the $|1, 0\rangle$ state, and one of the two $|1, 1\rangle$ states all map to the 3B_2 symmetry. The other one of the $|1, 1\rangle$ states and both of the $|2, 2\rangle$ states all map to the 3B_1 symmetry. Lastly, both of the $|2, 1\rangle$ states and the single $|2, 0\rangle$ state all map to the 3A_2 symmetry.

Putting this all together, the partition functions for the attractive 3B_2 , 3B_1 , and 3A_2 symmetries are given by

$$u_{3B_2} = u_0 + \frac{2}{3}u_1, \quad (39)$$

$$u_{3B_1} = \frac{1}{3}u_1 + \frac{2}{5}u_2, \quad (40)$$

$$u_{3A_2} = \frac{3}{5}u_2, \quad (41)$$

with u_J defined by Equation (12). The partition functions for the 3B_2 and 3B_1 symmetries are shown in Figure 14. The temperature dependence for the fractional population on attractive surfaces forming either of these ions is given by the factor

$$f = u_{3B_2} + u_{3B_1}, \quad (42)$$

which starts out at 1 at low temperature and decreases to $2/3$ at high temperature, as can be seen in Figure 14. The partition function of the repulsive 3A_2 symmetry is given by $1 - f$. All three partition functions converge to a value of $1/3$ at high temperature, i.e., for statistically populated J levels. Based on the above discussion and using these partition functions, we can develop all the scale factors needed to account for the temperature dependence of the fractional population on attractive surfaces.

Talbi et al. (1991) and Bettens & Collins (1998, 2001) find that the 3B_2 and 3B_1 symmetries both lead to $CH^+(a^3\Pi) + H_2$ formation. Calculations by Bettens & Collins (1998, 2001) indicate that the cross sections are the same for formation of CH^+ via the 3B_2 and 3B_1 symmetries. Furthermore, they find that ground-symmetry $CH_2^+(^2A_1)$ forms only via the $CH_3^+(^3B_2)$ surface.

The calculations of Bettens & Collins (1998, 2001), the measurements of Savić et al. (2005), and our results, all find that both the CH^+ and CH_2^+ channels are open. Thus the Langevin rate coefficient corresponds to the sum of the rate coefficients for these two channels. The temperature dependent Langevin thermal rate coefficient can then be written as

$$\alpha_{\text{L}}(T) = f(T)\alpha_{\text{L}}(T = 0), \quad (43)$$

The resulting temperature dependent Langevin rate coefficient is shown in Figure 15.

In order to convert our translational temperature results to thermal rate coefficients, we first add together the translational temperature rate coefficients for reactions (3) and (5) and multiply the sum by $\frac{3}{2}f$. This corrects our experimental data where only two-thirds of the C fine-structure levels contribute to the reaction process. Next we convert our results for CH_2^+ formation based on the predictions of Bettens & Collins (1998, 2001) that only the $^3\text{B}_2$ symmetry is involved. Hence, to derive the thermal rate coefficient for reaction (5) we need only multiply the translational temperature results by the factor $3u_{^3\text{B}_2}$. This corrects our experimental data where only one-third of the C fine-structure levels contribute to the formation of CH_2^+ . Lastly, for the thermal rate coefficient for reaction (3), we take the summed thermal rate coefficient for reactions (3) and (5) subtract from it that for reaction (5). The resulting thermal rate coefficients for reactions (3) and (5) are shown in Figure 15 and for the summed thermal rate coefficient in Figure 16.

9.4. Thermal Rate Coefficients

Our experimentally derived thermal rate coefficient for reaction (3) decreases with decreasing temperature. A comparison with the theoretical calculations of Talbi et al. (1991) and Bettens & Collins (1998, 2001), shown in Figure 15, finds poor agreement in both the magnitude and temperature dependence. At 10 K the calculations of Talbi et al. (1991) are

a factor of ≈ 6.6 greater than the experimental results. This discrepancy decreases with increasing temperature and is ≈ 3.3 at 300 K. Over this same temperature range, the calculations of Bettens & Collins (1998, 2001) lie a factor of ≈ 4.3 above ours at 10 K and ≈ 1.8 at 300 K. The current astrochemical databases (Wakelam et al. 2012; McElroy et al. 2013) use the Langevin rate coefficient for reaction (3). The unmodified and modified Langevin rate coefficients also do a poor job of reproducing our experimental results for this channel. This is not surprising since, as discussed above, the Langevin rate coefficient should be taken as representing the sum of the rate coefficients for reactions (3) and (5). Lastly, we note that the modified Langevin rate coefficient closely matches the calculations of Bettens & Collins (1998, 2001).

For reaction (5), our experimentally derived thermal rate coefficient increases with decreasing temperature. The theoretical calculations of Bettens & Collins (1998, 2001) show a roughly similar temperature dependence, but differ significantly in the magnitude of the rate coefficient. At 10 and 300 K, their calculations lie a respective factor of ≈ 51 and 29 times below our results. Theory appears to greatly underestimate the importance of this channel.

Above ~ 300 K the statistical fractional population in our experiment of the ground term $C(^3P_J)$ closely matches a thermal distribution. A similar situation is expected for the $\sim 3,000$ K carbon atoms in the Savić et al. (2005) measurements. Hence, we expect in both experiments that the corresponding CH_3^+ symmetries will be thermally populated. Thus, above 300 K our experimental rate coefficient remains essentially unchanged from that presented in Figure 12. As such, for formation of both CH^+ and CH_2^+ , there remains good agreement of our results with the mass-scaled experimental data from Savić et al. (2005).

We attribute all the differences between theory and our experimental results to a combination of factors. The first, as mentioned earlier, is that the potential energy surface of

the $C + H_3^+$ system is less attractive at large internuclear distances than currently predicted. Secondly, formation of CH_2^+ is over an order of magnitude easier than calculated by published theory. Lastly, these effects are amplified by the temperature dependence for the fractional population of reacting states.

The effects of the changing population of the attractive 3B_1 and 3B_2 symmetries can also be seen in the Figure 17 which shows the branching ratio for $C + H_3^+$ forming CH^+ and CH_2^+ . Formation of CH^+ dominates above ~ 50 K. Below this temperature the populations of the 3B_1 and 3A_2 symmetries decrease and all of the population shifts into the 3B_2 symmetry, reducing the rate coefficient for CH^+ formation and increasing that for CH_2^+ formation. In fact, our results predict that at the ~ 10 K temperature typical of dark molecular clouds approximately 80% of all $C + H_3^+$ reactions lead directly to CH_2^+ . This may be an issue for astrochemical models as this important channel is currently absent from astrophysical databases.

10. Some Astrophysical Implications

In gas-phase astrochemistry of dark molecular clouds, the CH_3^+ molecule is predicted to play a key role in the synthesis of complex organic molecules (Smith & Spanel 1995). Reaction (3) contributes to CH_3^+ formation via the hydrogen abstraction chain



On the scale of a dark cloud lifetime, the initial formation of CH^+ via reaction (3) is slow due to the low abundances of C and H_3^+ in the cloud. However, once the CH^+ molecule is formed it rapidly proceeds to CH_3^+ due to the high H_2 abundance and fast rate coefficient for the hydrogen abstraction reactions. Our thermal rate coefficient for reaction (3) at 10 K is significantly smaller than the unmodified Langevin value used in current astrochemical

databases (Wakelam et al. 2012; McElroy et al. 2013). At higher temperatures, it is still significantly reduced, suggesting a slower formation rate at higher temperatures for CH_3^+ from the $\text{C} + \text{H}_3^+$ pathway and thereby a reduced abundance of more complex organic molecules.

One needs, however, to also take into account reaction (5) which is currently not included in astrochemical models. This can lead to the formation of CH_3^+ via



which also proceeds rapidly for the same reasons as reaction pathway (44). We note reaction (45) also enables CH_2^+ formed via reaction (2) to go on to form CH_3^+ . Thus the rate coefficient for the reaction complex $\text{C} + \text{H}_3^+$ forming CH_3^+ is effectively the sum of the thermal rate coefficients for reactions (3) and (5).

Figure 15 shows the summed thermal rate coefficients for our results as well as the published theoretical and experimental results. Table 5 provides a numerical comparison at selected temperatures. The results of Talbi et al. (1991) always fall outside the estimated 1σ experimental uncertainty limits. The unmodified Langevin rate coefficient lies within these experimental limits from ~ 2 to 30 K. The modified Langevin results show reasonable agreement from ~ 2 to 60 K and are only slightly discrepant above ~ 60 K. Comparing to the summed results of Bettens & Collins (1998, 2001), we find surprisingly good agreement over most of the 10 – 300 K temperature range that they covered. Lastly, we continue to find good agreement with the experimental results of Savić et al. (2005).

Based on these comparisons, we expect that incorporating our results into astrochemical models will have a temperature-dependent effect on the gas-phase formation rate for CH_3^+ and the more complex organic molecules that are formed from CH_3^+ . At 10 K our summed rate coefficient for the reaction is in good agreement with the unmodified Langevin value currently used in the astrochemical databases. However, at 300 K, our summed value is a factor of ~ 2 lower. Determining the full astrochemical implications of our results will

require a detailed chemical simulation incorporating our findings, which is beyond the scope of our work here.

We also would like to point out that in molecular clouds, for densities of 10^4 cm^{-3} or higher, the population of the 3P_J levels is expected to be in thermal equilibrium. At lower densities the excitation of the J levels is probably less than thermal (Nussbaumer & Rusca 1979). It is clear that the field will eventually need fine-structure resolved rate coefficients.

11. Summary

We have developed a novel, merged fast-beams apparatus which allows us to merge a beam of molecular ions onto a neutral beam of ground-term atoms. Here we have described the apparatus in detail. For the proof-of-principle studies, we have measured the chemistry of $\text{C} + \text{H}_3^+$ forming CH^+ , CH_2^+ , and CH_3^+ . Our measurements were performed for statistically populated $\text{C}(^3P_J)$ in the ground term, which is nearly equivalent to the population expected for thermal temperatures above 300 K. Hence, our translational temperature results are expected to be similar to thermal results above this temperature. At $\sim 1,000$ K, we find good agreement between our results and the mass-scaled results from published ion trap measurements for $\text{C} + \text{D}_3^+$ forming CD^+ and CD_2^+ . At 300 K, our results for CH^+ formation lie a factor of $\sim 1.8 - 3.3$ below both the unmodified Langevin value currently in the astrochemical databases and the published semi-classical results. These databases do not currently include the CH_2^+ formation channel. Our translational temperature results at 300 K for forming CH_2^+ are a factor of ≈ 26.7 larger than the semi-classical results. Additionally, we have used statistical arguments as a guide to convert our translational temperature results to thermal results for temperatures below 300 K. Our conversion indicates that formation of CH_2^+ will dominate over that of CH^+ at temperatures below ~ 50 K. Clearly, though, further experimental work using cold H_3^+ molecules and more sophisticated theoretical calculations

are needed to test this prediction.

12. Acknowledgments

The authors thank E. Herbst, M. Delsaut, J. Liévin, B. J. McCall, E. F. McCormack, and P. C. Stancil for stimulating conversations. We also thank the referee for their insightful and helpful review. This work was supported in part by the Advanced Technologies and Instrumentation Program and the Astronomy and Astrophysics Grants Program in the NSF Division of Astronomical Sciences. X. Urbain is Senior Research Associate of the F.R.S.-FNRS.

REFERENCES

- Aberth, W. & Peterson, J. R. 1967, *Rev. Sci. Instrum.*, 38, 745
- Albertsson, T., Semenov, D. A., Vasyunin, A. I., Henning, T., & Herbst, E. 2013, *Astrophys. J. Suppl. Ser.*, 207, 27
- Althorpe, S. C. & Clary, D. C. 2003, *Annu. Rev. Phys. Chem.*, 54, 493
- Anicich, V. G. & Futrell, J. H. 1984, *Int. J. Mass Spectrom. Ion Proc.*, 55, 189
- Bettens, R. P. A. & Collins, M. A. 1998, *J. Chem. Phys.*, 108, 2424
- . 2001, *J. Chem. Phys.*, 114, 6490
- Bowman, J. M., Czakó, G., & Fu, B. 2011, *Phys. Chem. Chem. Phys.*, 13, 8094
- Brouillard, F. & Claeys, W. 1983, in *Physics of Ion-Ion and Electron-Ion Collisions* (New York: Plenum Press), 415–459

- Bruhns, H., Kreckel, H., Miller, K., Lestinsky, M., Seredyuk, B., Mitthumsiri, W., Schmitt, B. L., Schnell, M., Urbain, X., Rappaport, M. L., Havener, C. C., & Savin, D. W. 2010a, *Rev. Sci. Instrum.*, 81, 013112
- Bruhns, H., Kreckel, H., Miller, K. A., Urbain, X., & Savin, D. W. 2010b, *Phys. Rev. A*, 82, 042708
- Crandall, D. H., Ray, J. A., & Cisneros, C. 1975, *Rev. Sci. Instrum.*, 46, 562
- Delsaut, M. & Liévin, J. 2015, *J. Chem. Phys.*, in preparation
- Doucas, G. 1977a, *Int. J. Mass Spectrom. Ion Phys.*, 25, 71
- . 1977b, *Revue de Physique Appliquée*, 12, 1465
- Gay, C. D., Stancil, P. C., Lepp, S., & Dalgarno, A. 2011, *Astrophys. J.*, 737, 44
- Gentry, W. R. & Giese, C. F. 1977, *J. Chem. Phys.*, 67, 2355
- Gerlich, D. 2008, in *Low Temperature and Cold Molecules*, ed. I. W. M. Smith (London, UK: Imperial College Press), 121–174
- Gerlich, D., Borodi, G., Luca, A., & Mogo, C. Smith, M. A. 2011, *Phys. Chem. Chem. Phys.*, 225, 475
- Gerlich, D. & Horning, S. 1992, *Chem. Rev.*, 92, 1509
- Gioumousis, G. & Stevenson, D. P. 1958, *J. Chem. Phys.*, 29, 294
- Gu, X., Guo, Y., Kawamura, E., & Kaiser, R. 2006, *J. Vac. Sci. Technol. A*, 24, 505
- Guo, H. 2012, *Int. Rev. Phys. Chem.*, 31, 1
- Herbst, E. & Millar, T. J. 2008, in *Low Temperature and Cold Molecules*, ed. I. W. M. Smith (London, UK: Imperial College Press), 1–56

- Kaiser, R. I. & Suits, A. G. 1995, *Rev. Sci. Instrum.*, 66, 5405
- Klippenstein, S. J., Georgievskii, Y., & McCall, B. J. 2010, *J. Phys. Chem. A*, 114, 278
- Kreckel, H., Bruhns, H., Čížek, M., Glover, S. C. O., Miller, K. A., Urbain, X., & Savin, D. W. 2010, *Science*, 329, 69
- Kylänpää, I. & Rantala, T. T. 2011, *J. Chem. Phys.*, 135, 104310
- Li, A. & Guo, H. 2014, *J. Phys. C*, 118, 11168
- McElroy, D., Walsh, C., Markwick, A. J., Cordiner, M. A., Smith, K., & Millar, T. J. 2013, *Astron. & Astrophys.*, 550, A36
- McNab, I. R. 1995, *Adv. Chem. Phys.*, 89, 1
- Nussbaumer, H. & Rusca, C. 1979, *Astron. & Astrophys.*, 72, 129
- Rodgers, S. D. & Millar, T. J. 1996, *Mon. Not. R. Astron. Soc.*, 280, 1046
- Savić, I., Cermák, I., & Gerlich, D. 2005, *Int. J. Mass Spectrom.*, 240, 139
- Savin, D. W., Gardner, L. D., Reisenfeld, D. B., Young, A. R., & Kohl, J. L. 1995, *Rev. Sci. Instrum.*, 66, 67
- Scheer, M., Bilodeau, R. C., Brodie, C. A., & Haugen, H. K. 1998, *Phys. Rev. A*, 58, 2844
- Schuette, G. F. & Gentry, W. R. 1983, *J. Chem. Phys.*, 78, 1777
- Seman, M. L. & Branscomb, L. M. 1962, *Phys. Rev.*, 125, 1602
- Smith, D. & Spanel, P. 1995, *Mass Spectrometry Reviews*, 14, 255
- Staicu-Casagrande, E., Nzeyimana, T., Naji, E., de Ruelle, N., Fabre, B., Le Padellec, A., & Urbain, X. 2004, *Eur. Phys. J. D*, 31, 469

- Stancil, P. C., Lepp, S., & Dalgarno, A. 1998, *Astrophys. J.*, 509, 1
- Takao, T., Jinno, S., Hanada, K., Goto, M., Oshikiri, K., Okuna, K., Tanuma, H., Azuma, T., & Shiromaru, H. 2007, *J. Phys. Conf. Ser.*, 88, 6
- Talbi, D., Defrees, D. J., Egolf, D. A., & Herbst, E. 1991, *Astrophys. J.*, 374, 390
- Urbain, X., Cornet, A., Brouillard, F., & Giusti-Suzor, A. 1991, *Phys. Rev. Lett.*, 66, 1685
- van Dishoeck, E. F. 1998, in *The Molecular Astrophysics of Stars and Galaxies*, ed. T. W. Harquist and D. A. Williams (Oxford, UK: Clarendon Press), 53–99
- Vasyunin, A. I., Semenov, D., Henning, T., Wakelam, V., Herbst, E., & Sobolev, A. M. 2008, *Astrophys. J.*, 672, 629
- Wakelam, V., Herbst, E., Loison, J.-C., Smith, I. W. M., Chandrasekaran, V., Pavone, B., Adams, N. G., Bacchus-Montabonel, M.-C., Bergeat, A., Béroff, K., Bierbaum, V. M., Chabot, M., Dalgarno, A., van Dishoeck, E. F., Faure, A., Geppert, W. D., Gerlich, D., Galli, D., Hébrard, E., Hersant, F., Hickson, K. M., Honvault, P., Klippenstein, S. J., Le Picard, S., Nyman, G., Pernot, P., Schlemmer, S., Selsis, F., Sims, I. R., Talbi, D., Tennyson, J., Troe, J., Wester, R., & Wiesenfeld, L. 2012, *Astrophys. J. Suppl. Ser.*, 199, 21
- Wakelam, V., Loison, J.-C., Herbst, E., Talbi, D., Quan, D., & Caralp, F. 2009, *Astron. & Astrophys.*, 495, 513
- Wakelam, V., Smith, I. W. M., Herbst, E., Troe, J., Geppert, W., Linnartz, H., Öberg, K., Roueff, E., Agúndez, M., Pernot, P., Cuppen, H. M., Loison, J. C., & Talbi, D. 2010, *Space Sci. Rev.*, 156, 13
- Wilson, A. V., Parker, D. S. N., Zhang, F., & Kaiser, R. I. 2012, *Phys. Chem. Chem. Phys.*, 14, 477

Zhou, H. L., Manson, S. T., Hibbert, A., Ky, L. V., Feautrier, N., & Chang, J.-C. 2004,
Phys. Rev. A, 70, 022713

Table 1: Summary of typical statistical-like uncertainties going into Equation (11) for a single data run i . Also listed are the relevant symbols and their typical values. All uncertainties are quoted at a confidence level taken to be equivalent to a 1σ statistical confidence level, treated as random sign errors, and added in quadrature.

Source	Symbol	Section	Value	Uncertainty (%)
Signal rate	S	5	1-15 Hz	≤ 4
C velocity	v_n	3.1	$6.7 \times 10^7 \text{ cm s}^{-1}$	$\ll 1$
H_3^+ velocity	v_i	3.2	$6.7 \times 10^7 \text{ cm s}^{-1}$	$\ll 1$
C current	I_n	3.5	30 nA	5
H_3^+ current	I_i	3.3	200 nA	5
Overlap factor	$\langle \Omega(z) \rangle$	4	2.7 cm^{-2}	10
Statistical-like uncertainty (single run)				13

Table 2: Same as Table 1 but for the systematic uncertainties for all runs.

Source	Symbol	Section	Value	Uncertainty (%)
Analyzer transmission	T_a	3.4	0.73	3
Grid transmission	T_g	3.4	0.90	1
Neutral transmission	T_n	3.5	0.94	2
Neutral detector calibration	γ	3.5	2.7	11
CEM efficiency	η	3.6	0.99	3
Interaction length	L	3.3	121.5 cm	2
Total systematic uncertainty				12

Table 3: Fit parameters for the cross sections of reactions (3) and (5) vs. relative energy.

The resulting cross sections using Equation (28) are in units of cm^2 for E given in eV.

Reaction	Parameters				
	a_0	$a_{1/2}$	b_1	b_2	b_4
(3)	2.3474E-16	1.1028E-15	-	1.4694E-01	2.0471E-03
(5)	1.9983E-16	-	5.4737E-02	5.6944E-03	2.2891E-01

Table 4: Fit parameters for the translational temperature rate coefficients for reactions (3) and (5). The resulting rate coefficients from Equation (29) are in units of $\text{cm}^3 \text{s}^{-1}$ for T given in K.

Reaction	Parameters					
	a_0	$a_{1/2}$	a_1	$b_{1/2}$	b_1	$b_{3/2}$
(3)	1.0218E-09	7.2733E-11	5.9203E-14	4.4914E-02	-2.6056E-04	2.6397E-06
(5)	8.5145E-10	-	-	9.5666E-04	-4.4040E-05	2.3496E-06

Table 5: Summed thermal rate coefficients for $\text{C} + \text{H}_3^+$ forming both CH^+ and CH_2^+ for selected temperatures. The rate coefficients are given in units of $10^{-9} \text{ cm}^3 \text{ s}^{-1}$.

Source	Temperature (K)						
	10	20	50	100	200	300	1000
Langevin (unmodified)	2.0	2.0	2.0	2.0	2.0	2.0	2.0
Langevin (modified)	2.0	1.9	1.6	1.5	1.4	1.4	1.3
Talbi et al. (1991)	2.9	3.0	2.8	2.6	2.4	2.3	
Bettens & Collins (1998, 2001)	1.9	1.8	1.5	1.4	1.4	1.3	
Savić et al. (2005)							0.9 ± 0.3
Present results	2.0 ± 0.4	1.8 ± 0.4	1.4 ± 0.3	1.2 ± 0.2	1.1 ± 0.2	1.1 ± 0.2	1.0 ± 0.2

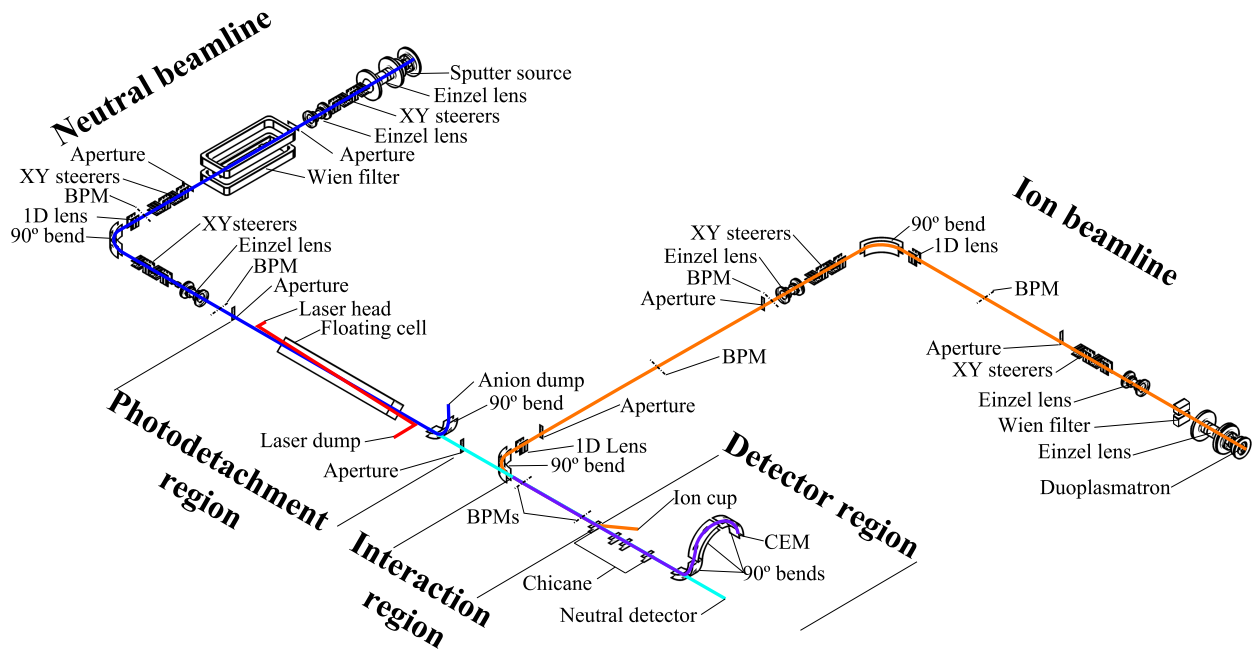


Fig. 1.— Overview of the merged-beams apparatus.

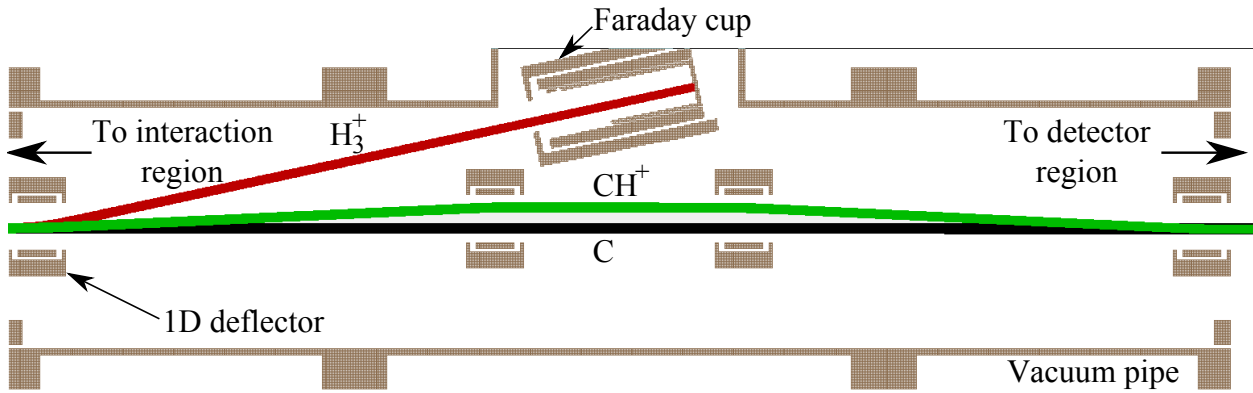


Fig. 2.— SIMION model of the chicane showing the demerging of the ion beams using a series of parallel-plate 1D deflectors, only the first one of which is labeled. The H_3^+ is directed upwards into a Faraday cup and the current recorded. The CH^+ beam is then re-merged with the C beam and directed into an electrostatic energy analyzer. Any CH_2^+ or CH_3^+ will be deflected less strongly than the CH^+ beam.

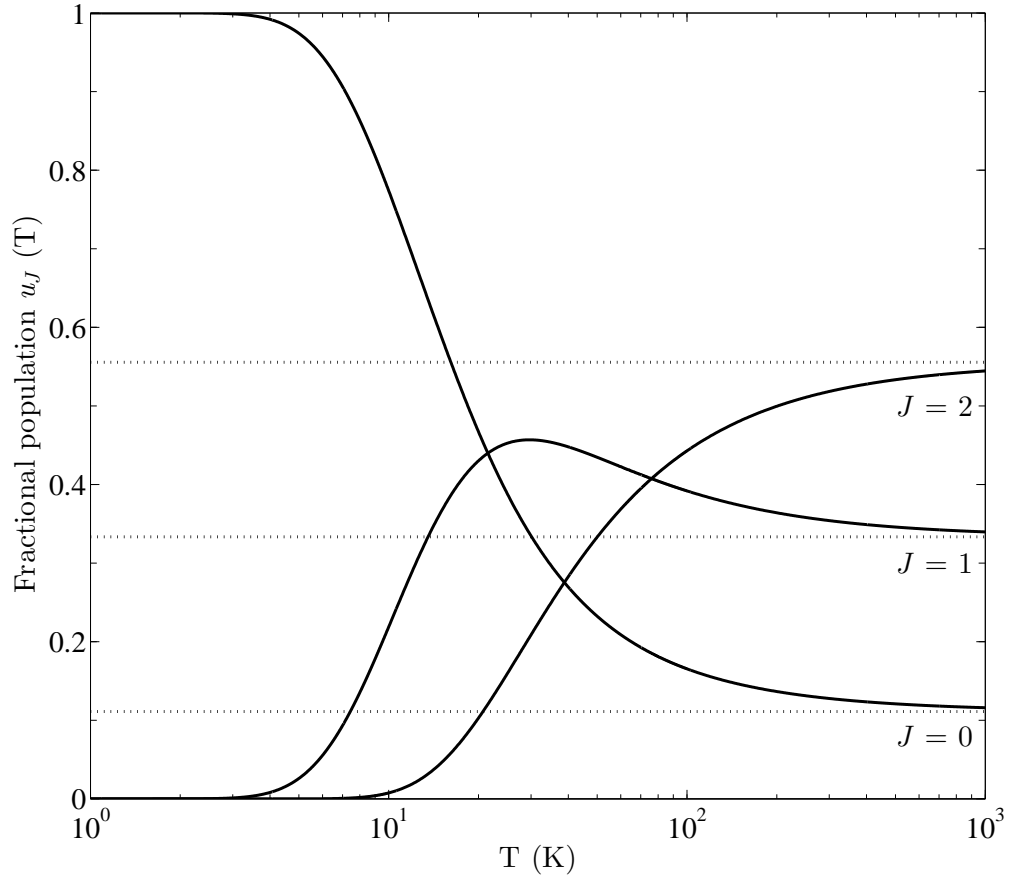


Fig. 3.— Fractional population of the 3P_J levels for a thermal distribution (solid curves) and a statistical distribution (dotted lines).

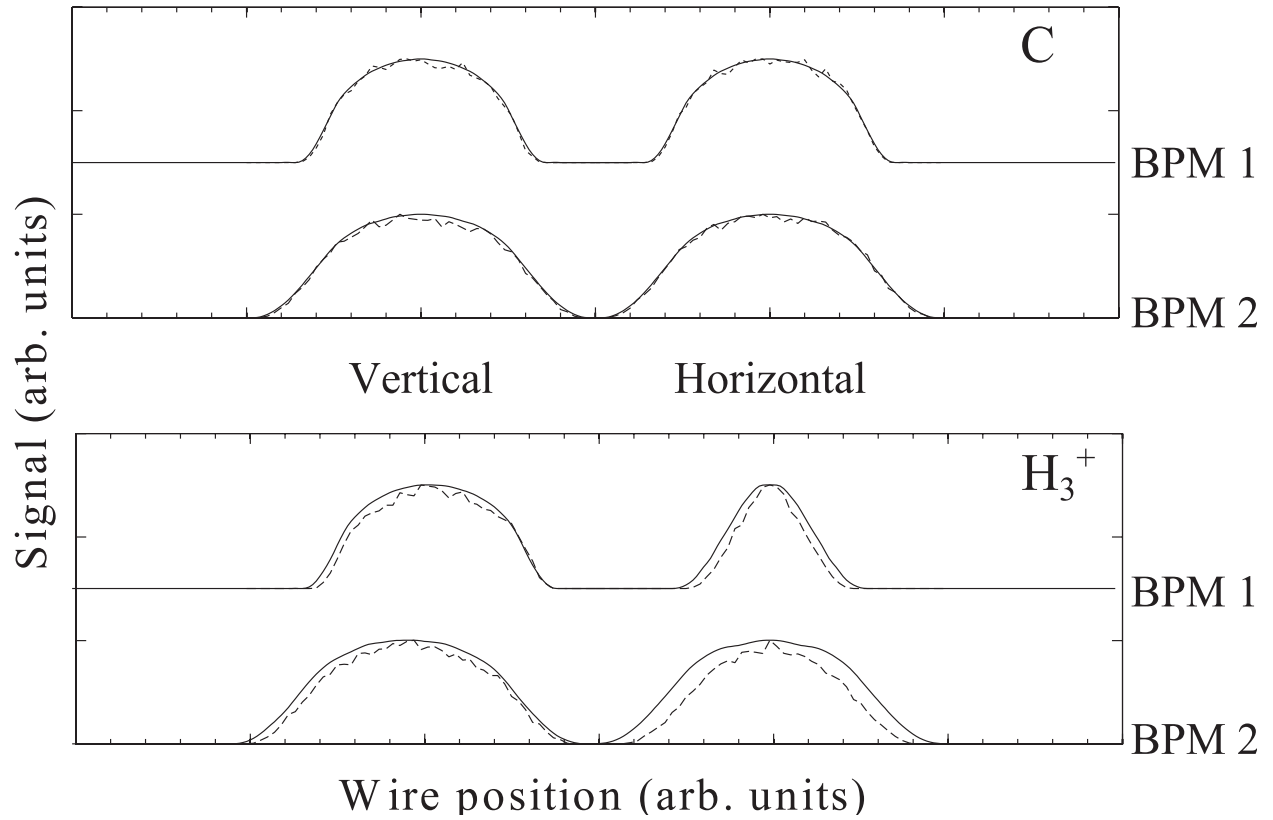


Fig. 4.— Comparison between the experimental profiles (dashed lines) and simulated profiles (solid lines) at BPM 1 and 2, respectively positioned 280 and 1090 mm from the start of the interaction region. Profiles are shown for both the C and H₃⁺ beams.

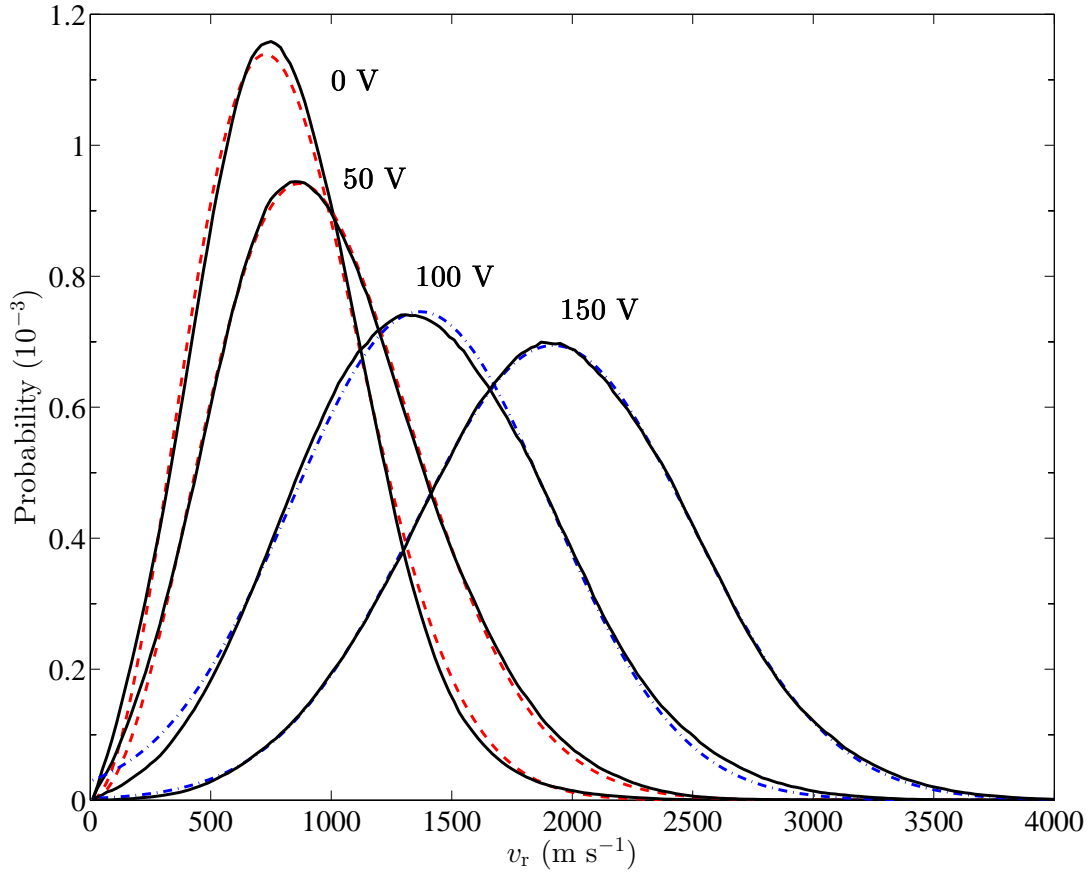


Fig. 5.— Relative velocity distribution for selected values of the floating cell voltage $|U_f|$. The solid curves show the results for $|U_f| = 0, 50, 100,$ and 150 V. The dashed curves are ≈ 72 and 109 K Maxwell-Boltzmann distributions which provided the best fits to the 0 and 50 V, data respectively. The Gaussian fits of the 100 and 150 V results (dotted curves) are also shown.

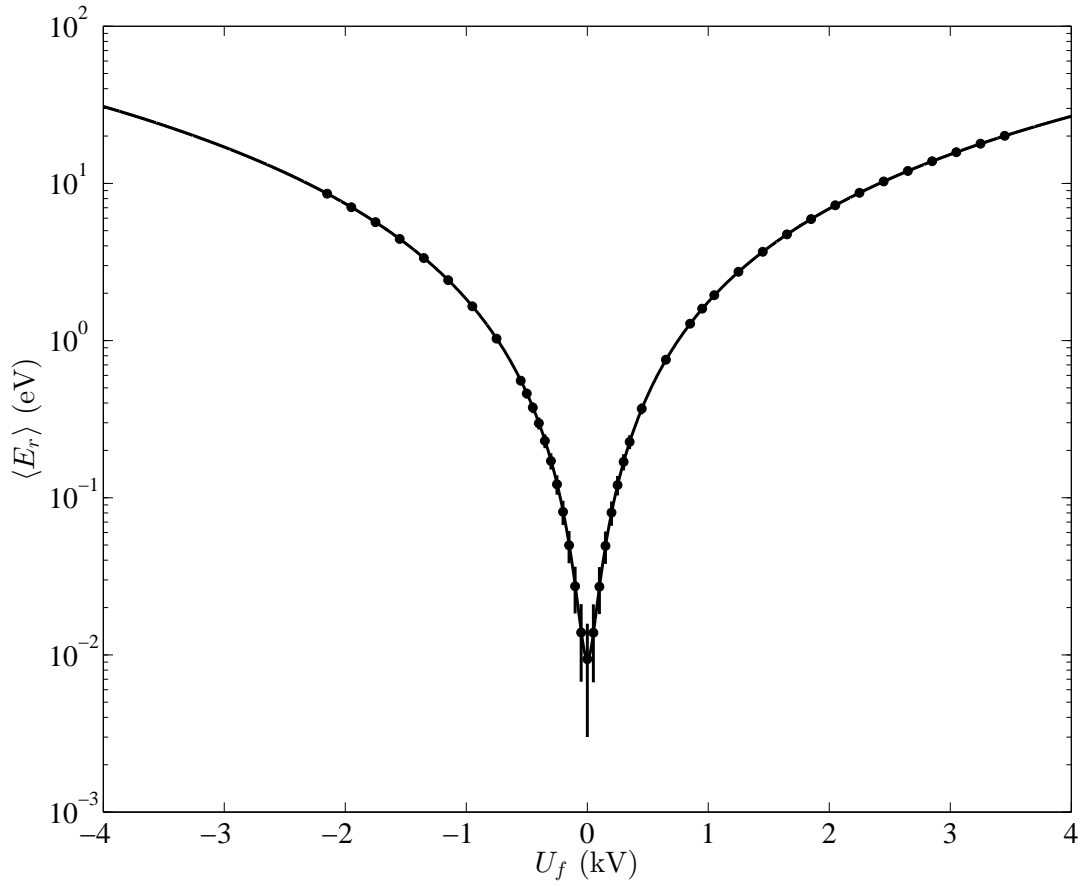


Fig. 6.— Simulated average relative energy $\langle E_r \rangle$ as a function of the floating cell voltage U_f . Vertical error bars on the filled circles indicate the FWHM spread of the modeled distribution. The solid line is the calculation for the average relative energy derived from Equation (10).

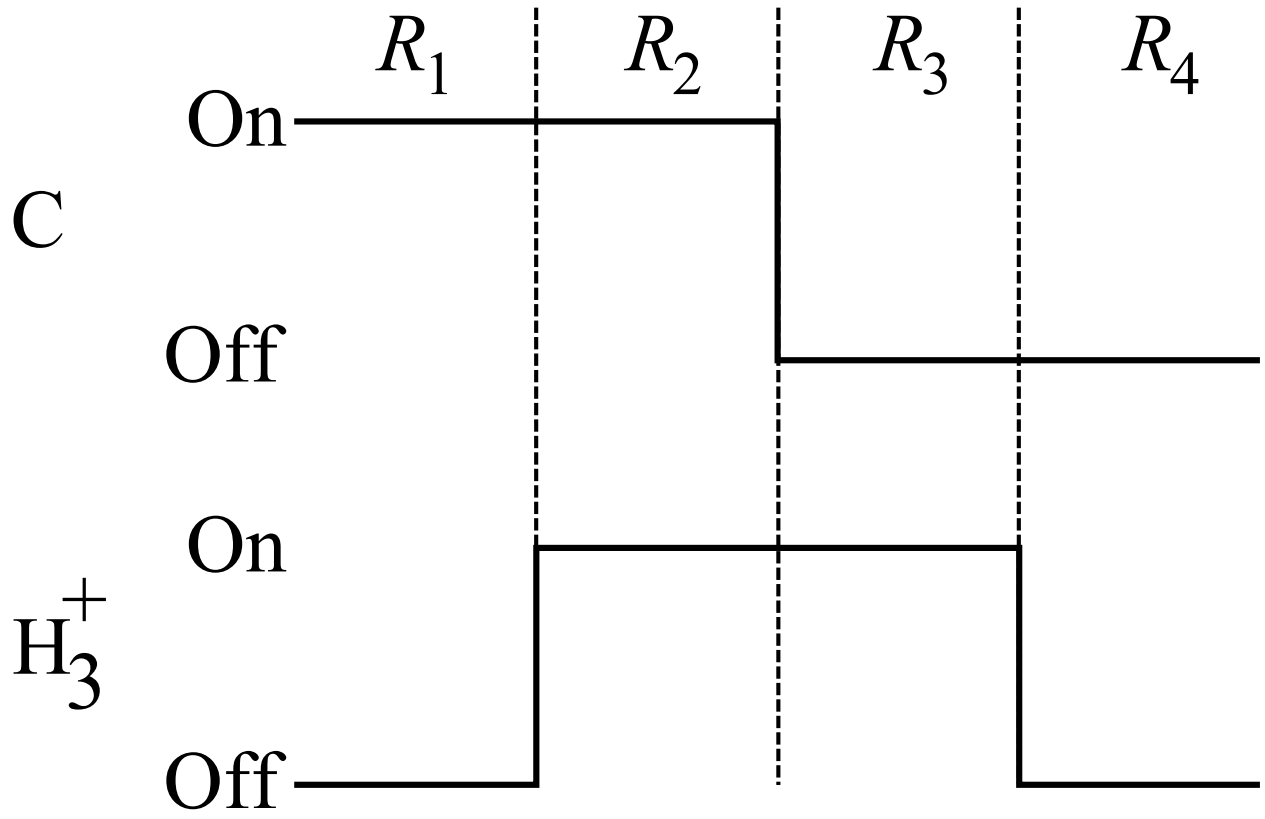


Fig. 7.— Data acquisition timing sequence.

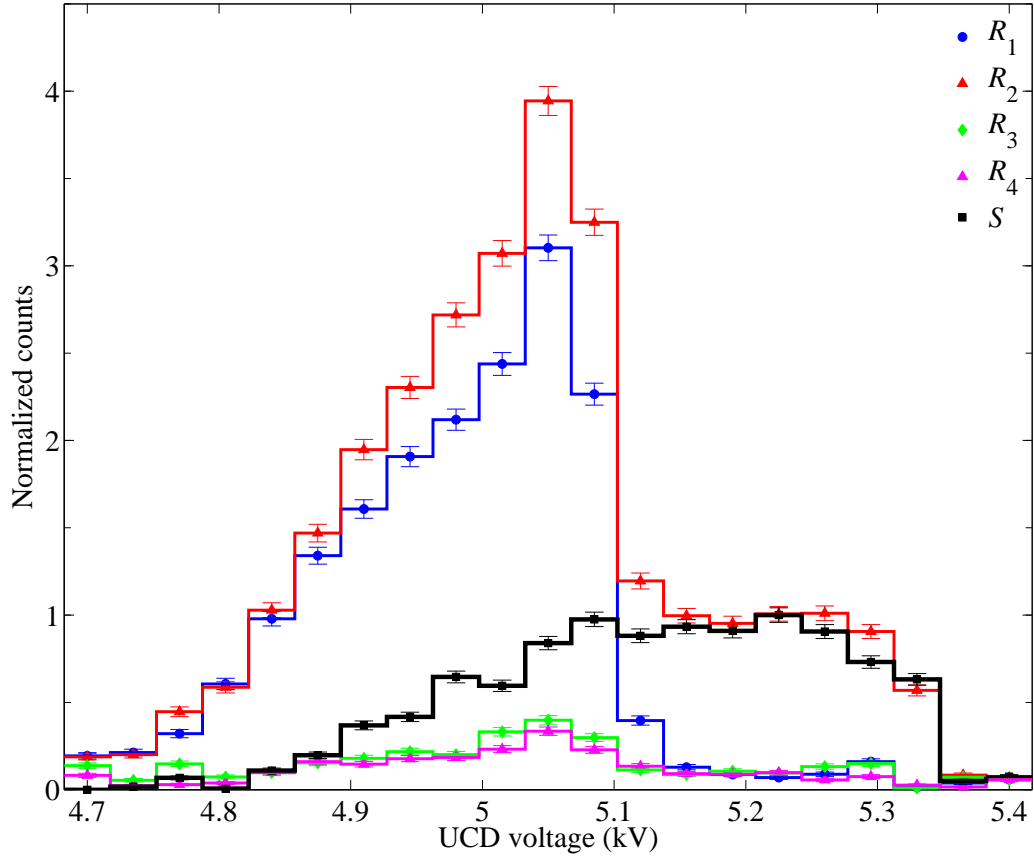


Fig. 8.— UCD scans of rates R_1 through R_4 and the resulting extracted signal S . The data have been normalized so that the peak in S is 1. The error bars show the 1σ counting-statistics uncertainty on each point.

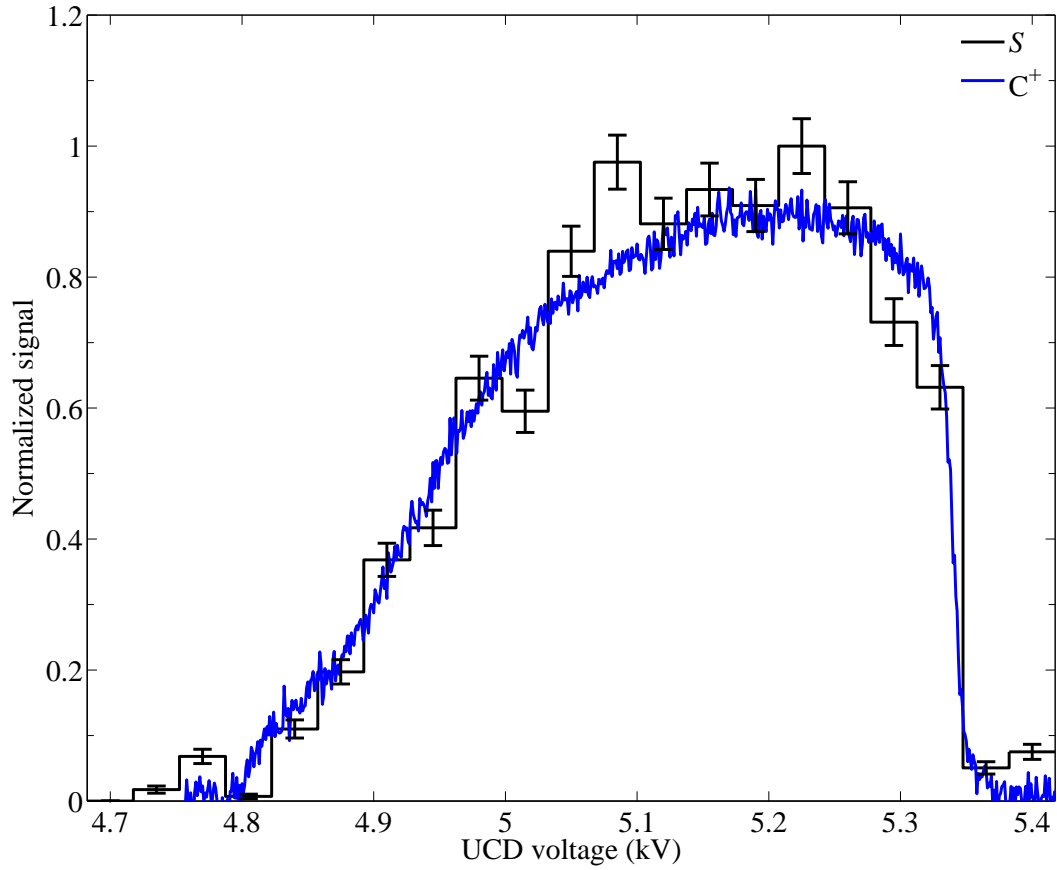


Fig. 9.— UCD voltage scan of a C^+ beam current, with a kinetic energy tuned to act as a proxy for the CH^+ signal. Also shown is the measured signal count rate S and associated 1σ counting-statistics uncertainty. S has been normalized to 1 at the peak value and the C^+ current has been scaled to best show the agreement in the structure between the two.

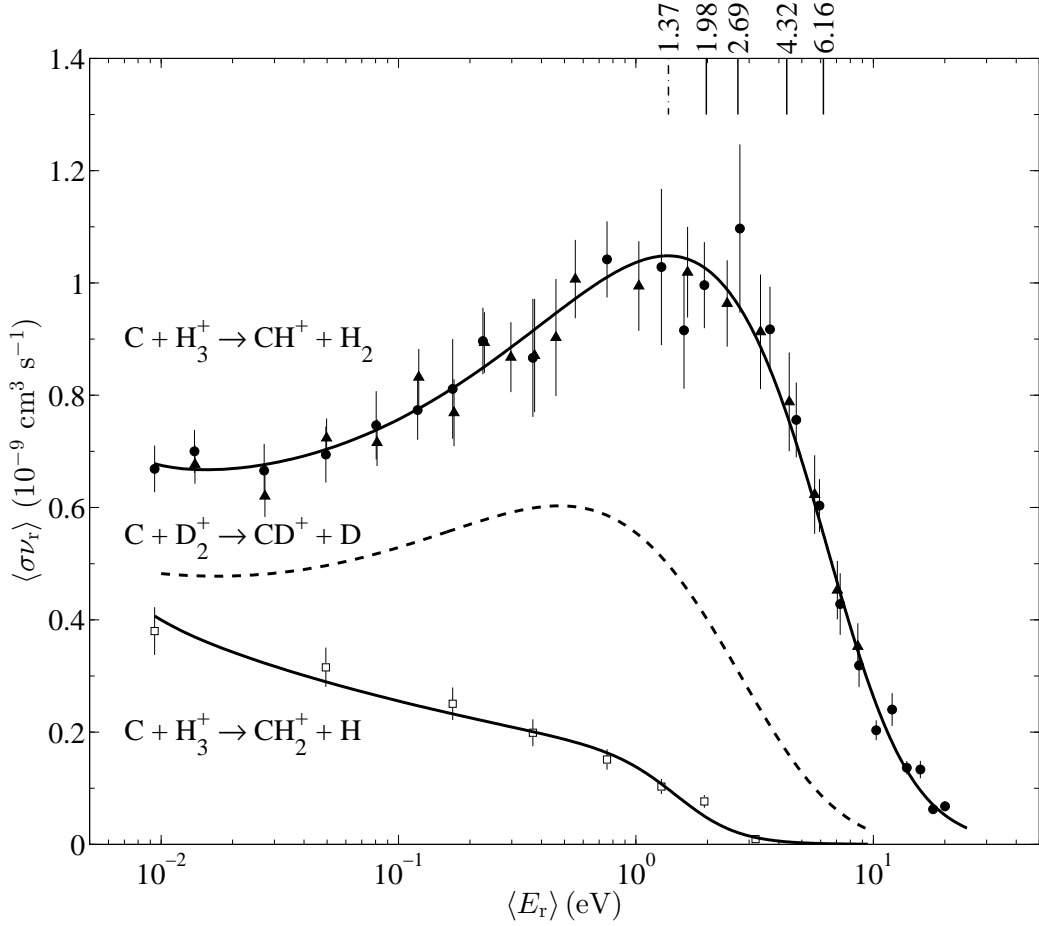


Fig. 10.— Experimental merged-beams rate coefficient $\langle \sigma v_r \rangle$ as a function of the average relative energy $\langle E_r \rangle$ for reaction (3) forming $\text{CH}^+ + \text{H}_2$ (filled symbols) and reaction (5) forming $\text{CH}_2^+ + \text{H}$ (open symbols). The circles denote $v_C \geq v_{\text{H}_3^+}$ and the triangles $v_C < v_{\text{H}_3^+}$ for reaction (3). The error bars signify the 1σ statistical-like uncertainty. The solid lines are an empirical fit to the experimental data using Equation (28). For comparison, the dashed line shows the measured experimental rate coefficient of Schuette & Gentry (1983) for reaction (9): $\text{C} + \text{D}_2^+ \rightarrow \text{CD}^+ + \text{D}$. The solid vertical lines denote energies at which the competing reactions (32), (33), (34), and (35) open at $\approx 1.98, 2.69, 4.32,$ and 6.16 eV, respectively. The dot-dashed vertical line denotes the energy at which the experimental rate coefficient is inferred to peak, approximately 0.61 eV below the first competing channel.

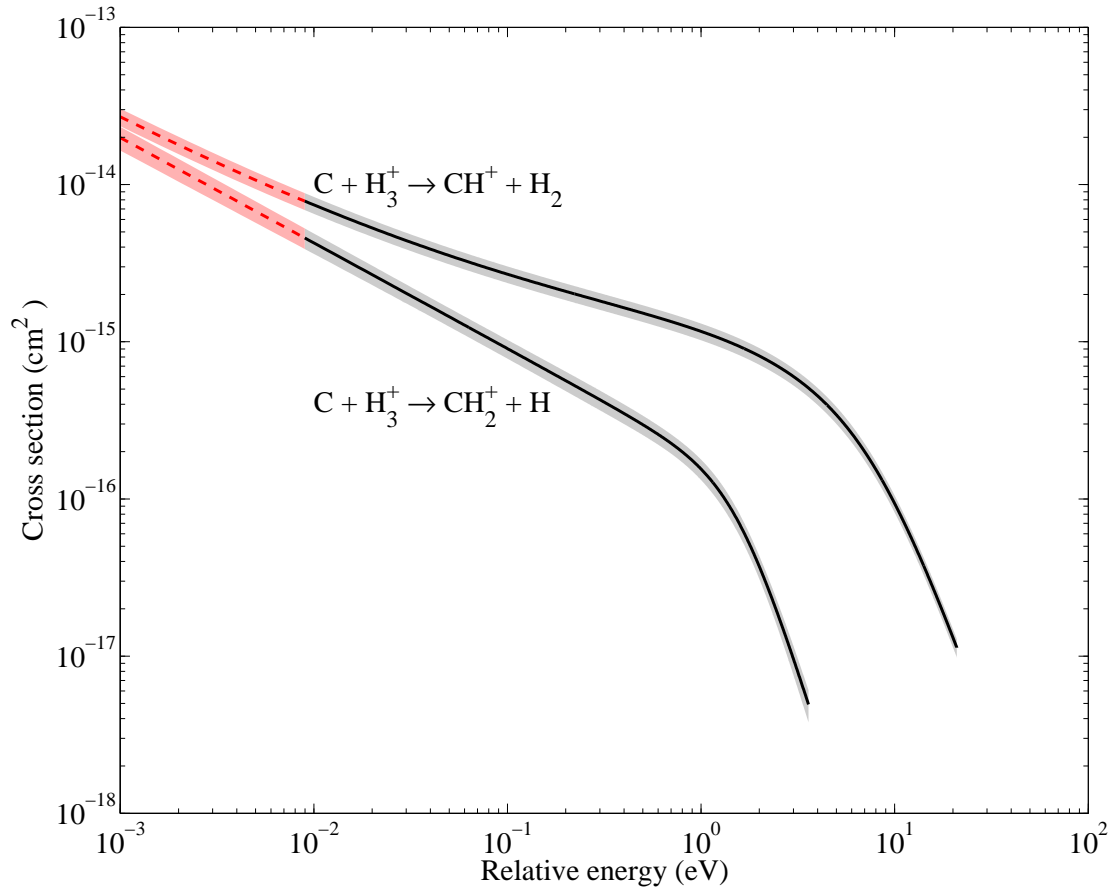


Fig. 11.— Experimentally derived cross sections as a function of relative energy for reactions (3) and (5) are shown by the solid black lines. The shaded areas signify the quadrature sum of the systematic uncertainty and fitting accuracy. The red lines use the fits to extrapolate the experimental results to lower impact energies and the surrounding shaded region assumes a constant uncertainty given by that at the lowest measured energy.

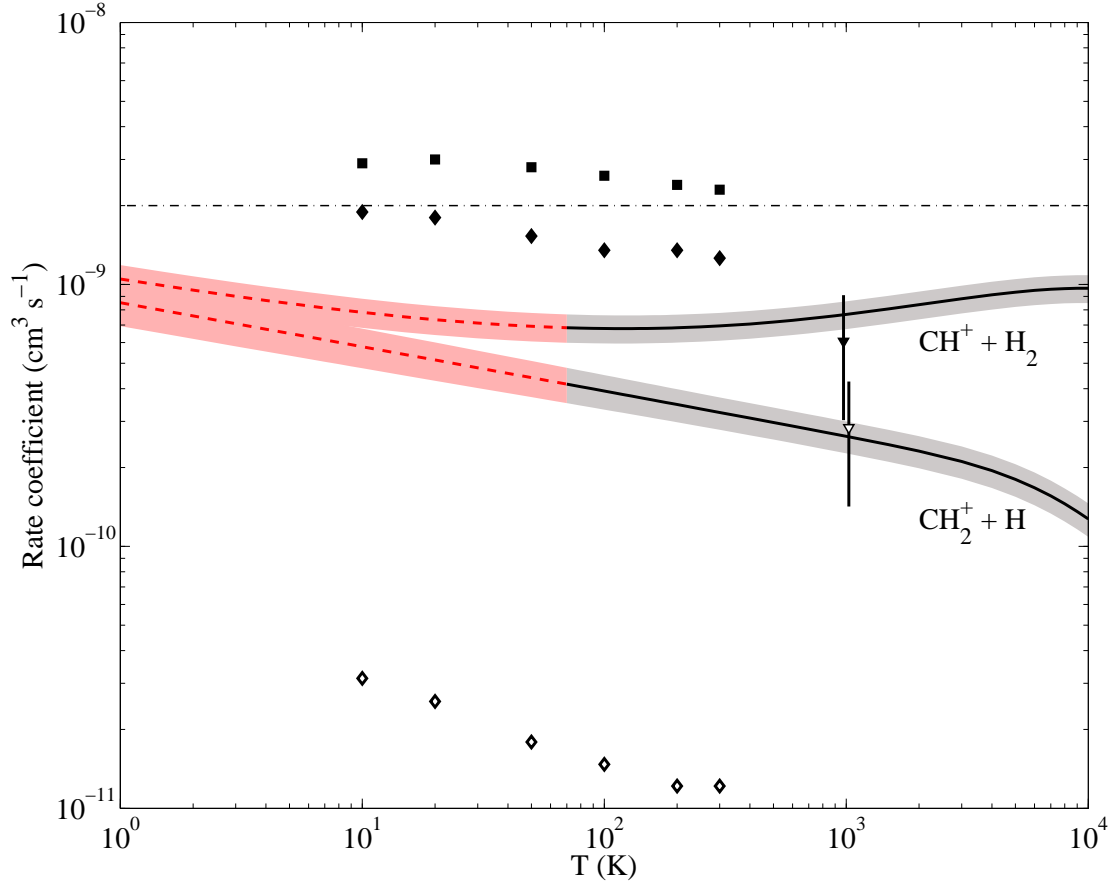


Fig. 12.— The black solid lines present our experimentally derived translational temperature rate coefficient for $C + H_3^+ \rightarrow CH^+ + H_2$, reaction (3), and $C + H_3^+ \rightarrow CH_2^+ + H$, reaction (5). The quadrature sum of the systematic uncertainty and fitting accuracy is denoted by the shaded region. The red dashed lines extrapolate these results to lower temperatures and the surrounding shaded area assumes a constant systematic uncertainty given by that at the lowest measured temperature added in quadrature to the accuracy of the fit. The dot-dashed curve shows the Langevin rate coefficient. The theoretical thermal rate coefficients of Talbi et al. (1991) and Bettens & Collins (1998, 2001) are shown by the squares and diamonds, respectively. The full and open symbols denote the results for reactions (3) and (5), respectively. The inverted triangles give the experimental result of Savić et al. (2005) for the fully deuterated isotopologues for these reactions, but scaled by the reduced mass for $C + H_3^+$ collision system. Their results are at an estimated translational temperature of $\sim 1,000$ K and for clarity have been shifted by ∓ 25 K, respectively.

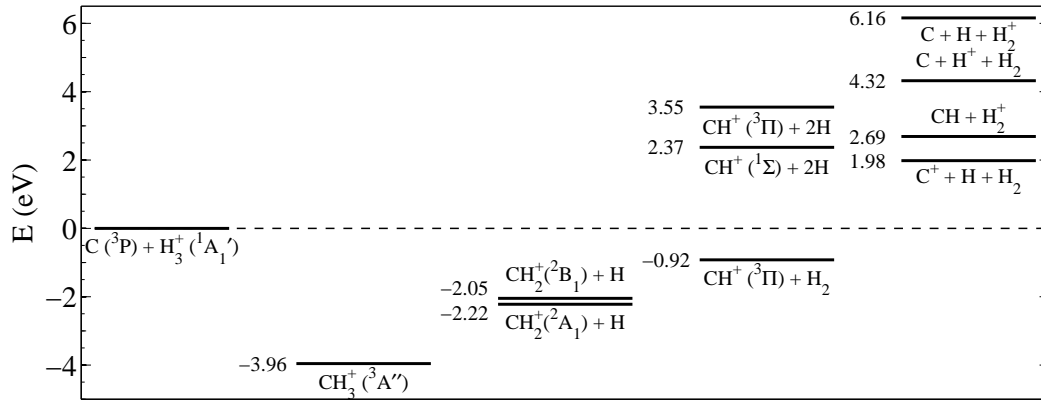


Fig. 13.— Energy-level diagram for various $C + H_3^+$ reaction pathways, as given by Delsaut & Liévin (2015)

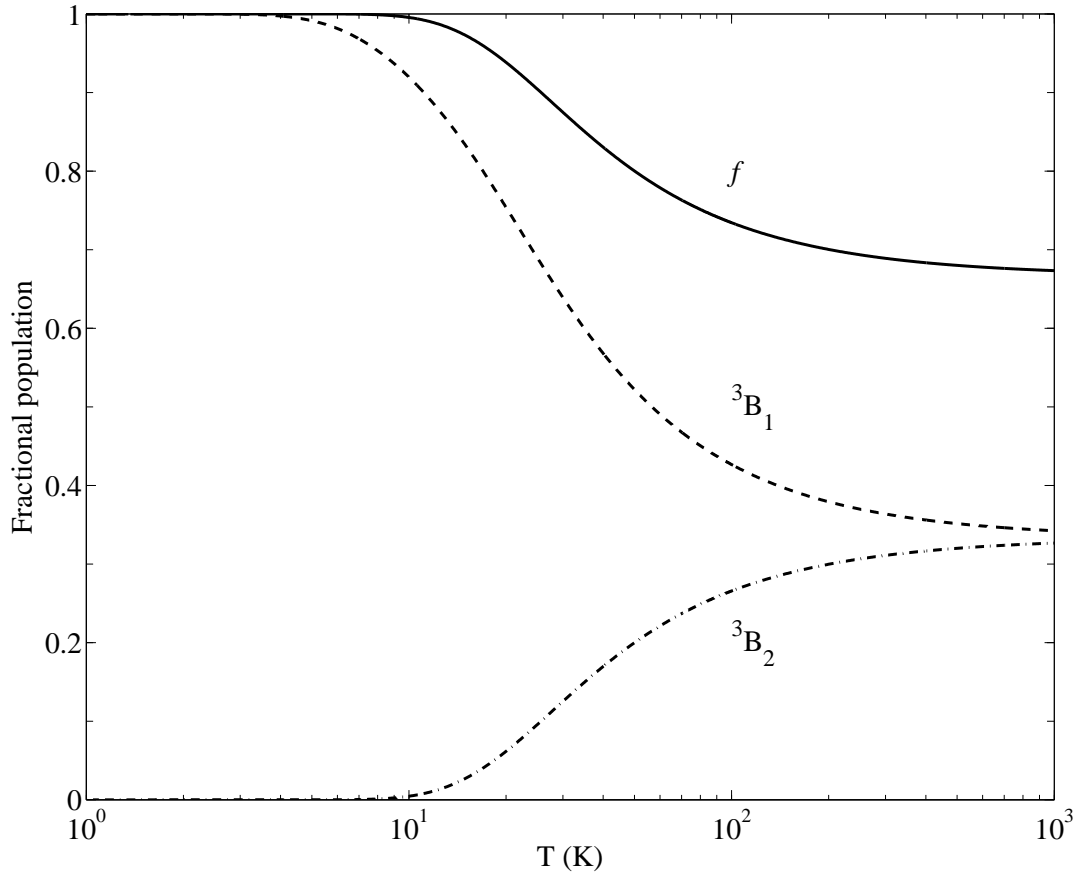


Fig. 14.— Fractional population of the two lowest CH_3^+ reactive triplet symmetries and their sum f versus temperature.

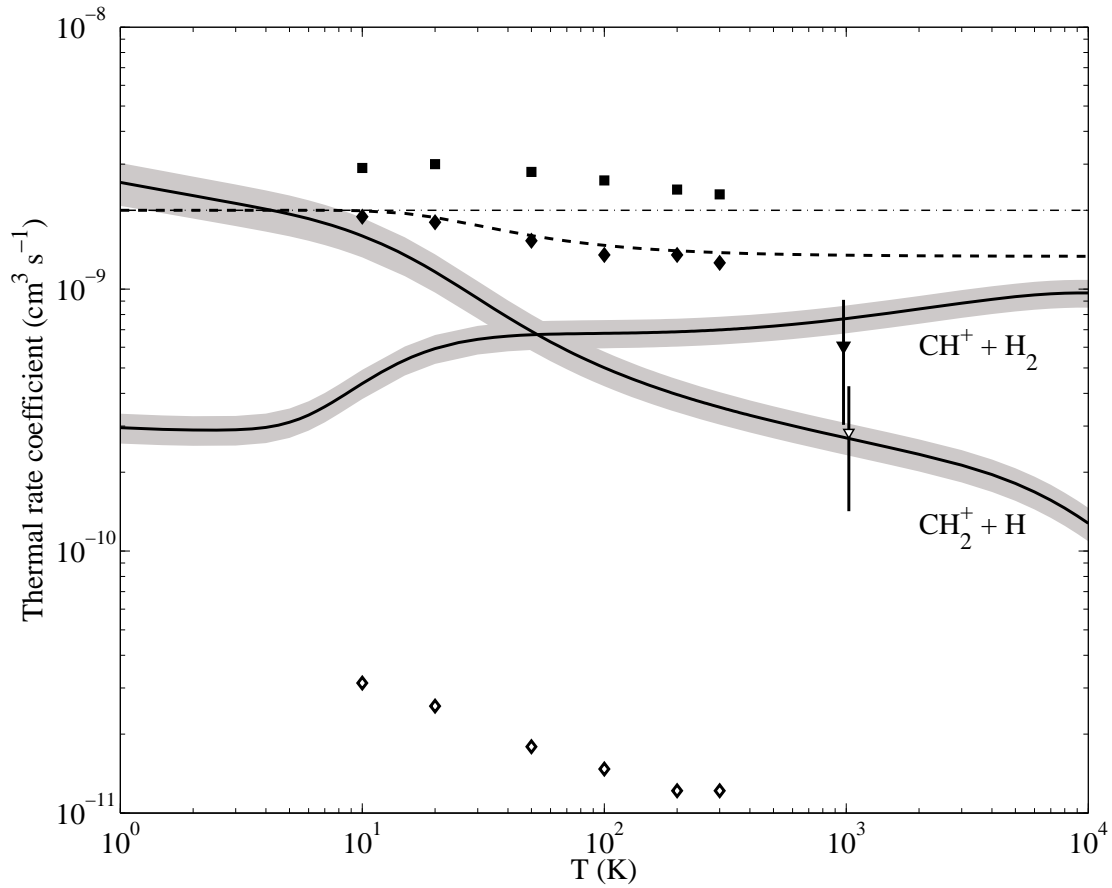


Fig. 15.— The solid curves represents our experimentally derived thermal rate coefficients as described in Section 9.3. The shaded areas show the estimated 1σ total experimental uncertainty. The dashed curve is the modified Langevin value, given by Equation (43). All other theoretical and experimental results are the same as in Figure 12.

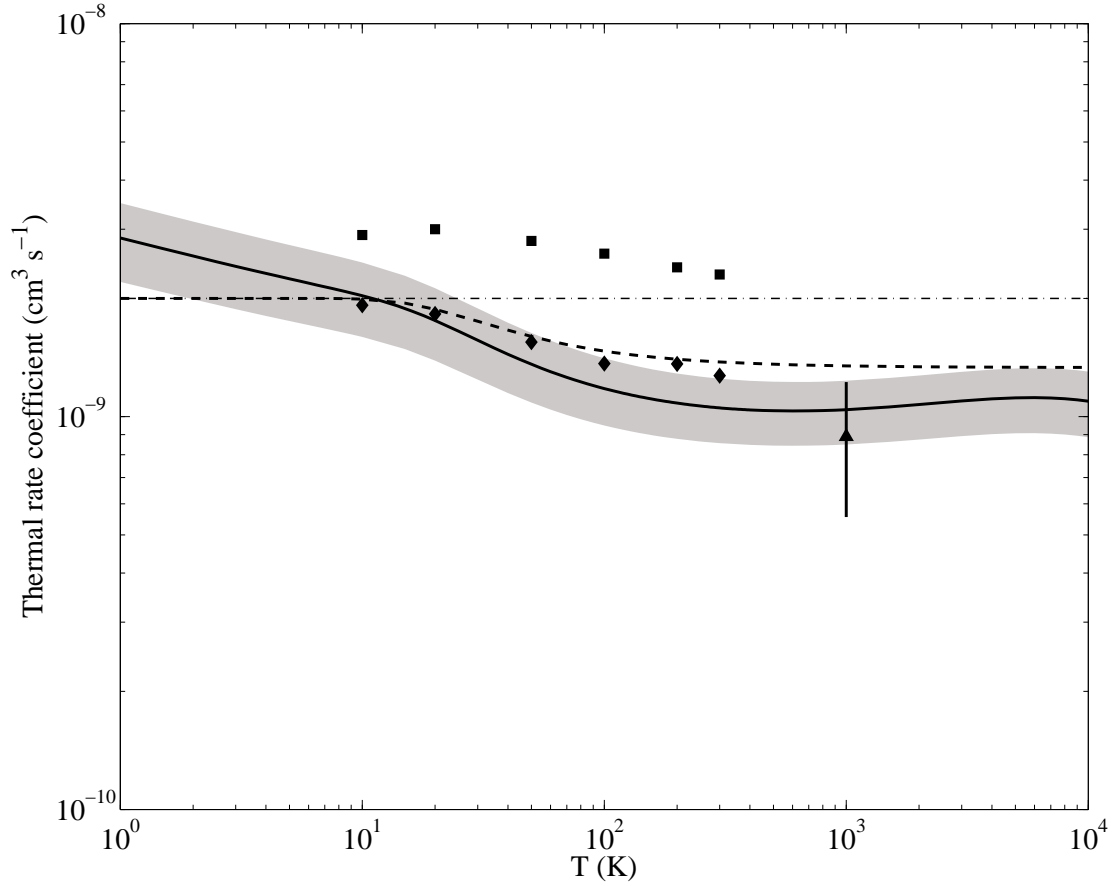


Fig. 16.— Summed thermal rate coefficients for $C + H_3^+$ forming both CH^+ and CH_2^+ . The solid curve presents our experimentally derived results and the shaded area the quadrature sum of the errors shown in Figure 15. The dot-dashed curve shows the unmodified Langevin rate coefficient and the dashed curve the modified value. The squares present the theoretical results of Talbi et al. (1991) and the diamonds those of Bettens & Collins (1998, 2001). The triangle gives the mass-scaled experimental results of Savić et al. (2005).

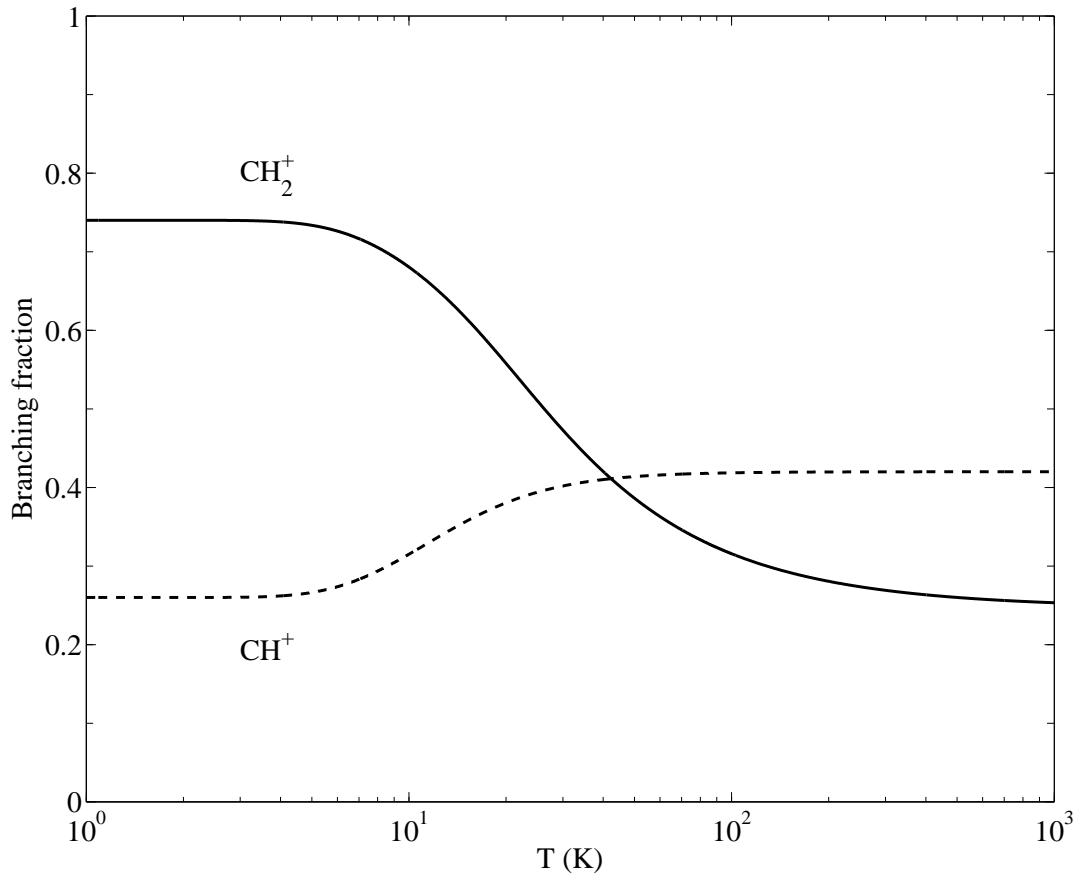


Fig. 17.— Temperature dependent branching fractions for the $\text{C} + \text{H}_3^+$ reaction forming CH^+ and CH_2^+ .